hunchback PROMOTERS CAN READOUT MORPHOGENETIC POSITIONAL INFORMATION IN LESS THAN A MINUTE

A PREPRINT

Jonathan Desponds
Department of Physics
University of California, San Diego
La Jolla, California, United States of America

Massimo Vergassola
Department of Physics
University of California, San Diego
La Jolla, California, United States of America

Aleksandra M. Walczak
Laboratoire de Physique, Ecole Normale Supérieure,
PSL Research University, CNRS, Sorbonne Université
Paris, France

June 21, 2019

ABSTRACT

The first cell fate decisions in the developing fly embryo are made very rapidly : *hunchback* genes decide in a few minutes whether a given nucleus follows the anterior or the posterior developmental blueprint by reading out the positional information encoded in the Bicoid morphogen. This developmental system constitutes a prototypical instance of the broad spectrum of regulatory decision processes that combine speed and accuracy. Traditional arguments based on fixed-time sampling of Bicoid concentration indicate that an accurate readout is not possible within the short times observed experimentally. This raises the general issue of how speed-accuracy tradeoffs are achieved. Here, we compare fixed-time sampling strategies to decisions made on-the-fly, which are based on updating and comparing the likelihoods of being at an anterior or a posterior location. We found that these more efficient schemes can complete reliable cell fate decisions even within the very short embryological timescales. We discuss the influence of promoter architectures on the mean decision time and decision error rate and present concrete promoter architectures that allow for the fast readout of the morphogen. Lastly, we formulate explicit predictions for new experiments involving Bicoid mutants.

***K*eywords** Regulation · Biological decisions · Speed-accuracy · Morphogenesis · *Drosophila* · Cell fate

0 Introduction

From development to chemotaxis and immune response, living organisms make precise decisions based on limited information cues and intrinsically noisy molecular processes, such as the readout of ligand concentrations by specialized genes or receptors [1, 2, 3, 4, 5]. Selective pressure in biological decision-making is often strong, for reasons that range from predator evasion to growth maximisation or fast immune clearance. In development, early embryogenesis of insects and amphibians unfolds outside of the mother, which arguably imposes selective pressure for speed to limit the risks of predation and infection by parasitoids [6]. In *Drosophila* embryos, the first 13 cycles of DNA replication and mitosis occur without cytokinesis, resulting in a multinucleated syncytium containing about 6,000 nuclei [7]. Speed is witnessed both by the rapid and synchronous cleavage divisions observed over the cycles, and the successive fast decisions on the choice of differentiation blueprints, which are made in less than 3 minutes [8].

In the early fly embryo, the map of the future body structures is set by the segmentation gene hierarchy [9, 1, 10]. The definition of the positional map starts by the emergence of two (anterior and posterior) regions of distinct *hunchback* (*hb*) expression, which are driven by the readout of the maternal Bicoid (Bcd) morphogen gradient (Fig. 1 A). *hunchback*

spatial profiles are sharp and the variance in *hunchback* expression of nuclei at similar positions along the AP axis is small [11, 8]. Taken together, these observations imply that the short-time readout is accurate and has a low error. Accuracy ensures spatial resolution and the correct positioning of future organs and body structures, while low errors ensure reproducibility and homogeneity among spatially close nuclei. The amount of positional information available at the transcriptional locus is close to the minimal amount necessary to achieve the required precision [12, 13, 14, 15]. Furthermore, part of the morphogenetic information is not accessible for reading by downstream mechanisms [16], as information is channeled and lost through subsequent cascades of gene activity. In spite of that, by the end of nuclear cycle 14 the positional information encoded in the gap gene readouts is sufficient to correctly predict the position of each nucleus within 2% of the egg length [15]. Adding to the time constraints, mitosis resets the binding of transcription factors (TF) during the phase of synchronous divisions, suggesting that the decision about the nuclei's position is made by using information accessible within one nuclear cycle. Experiments additionally show that during the nuclear cycles 10-13 the positional information encoded by the Bicoid gradient is read out by *hunchback* promoters precisely and within 3 minutes.

Effective speed-accuracy tradeoffs are not specific to developmental processes, but are shared by a large number of sensing processes. This generality has triggered interest in quantitative limits and mechanisms for accuracy. Berg and Purcell derived the seminal tradeoff between integration time and readout accuracy for a receptor evaluating the concentration of a ligand [17] based on its average binding occupancy. Later studies showed that this limit takes more complex forms when rebinding events of detached ligands [18, 19] or spatial gradients [20] are accounted for. The accuracy of the averaging method in [17] can be improved by computing the maximum likelihood estimate of the time series of receptor occupancy for a given model [21, 22]. However, none of these approaches can result in a precise anterior-posterior (AP) decision for the *hunchback* promoter in the short time of the early nuclear cycles, which has led to the conclusion that there is not enough time to apply the fixed-time Berg-Purcell strategy with the desired accuracy [23]. Additional mechanisms to increase precision (including internuclear diffusion) do yield a speed-up [24, 25], yet they are not sufficient to meet the 3 minutes challenge. The issue of the embryological speed-accuracy tradeoff remains open.

The approaches described above are fixed-time strategies of decision-making, i.e., they assume that decisions are made at a pre-defined deterministic time T that is set long enough to achieve the desired level of error and accuracy. As a matter of fact, fixing the decision time is not optimal because the amount of available information depends on the specific statistical realization of the noisy signal that is being sensed. The time of decision should vary accordingly and therefore depend on the realization. This intuition was formalized by A. Wald by his Sequential Probability Ratio Test (SPRT) [26]. SPRT achieves optimality in the sense that it ensures the fastest decision strategy for a given level of expected error. The adaption of the method to biological sensing posits that the cell discriminates between two hypothetical concentrations by accumulating information through binding events, and by computing on the fly the ratio of the likelihoods (or appropriate proxies) for the two concentrations to be discriminated [27]. When the ratio "strongly" favors one of the two hypotheses, a decision is triggered. The strength of the evidence required for decision-making depends on the desired level of error. For a given level of precision, the average decision time can be substantially shorter than for traditional averaging algorithms [27]. SPRT has also been proposed as an efficient model of decision-making in the fields of social interactions and neuroscience [28, 29] and its connections with non-equilibrium thermodynamics are discussed in [30].

Wald's approach is particularly appealing for biological concentration readouts since many of them, including the anterior-posterior decision faced by the *hunchback* promoter, appear to be binary decisions. Our first goal here is to specifically consider the paradigmatic example of the *hunchback* promoter and elucidate the degree of speed-up that can be achieved by decisions on the fly. Second, we investigate specific implementations of the decision strategy in the form of possible *hunchback* promoter architectures. We specifically ask how cooperative TF binding affects the sensing limits. Our results have implications beyond fly development and are generally relevant to regulatory processes. We identify promoter architectures that, by approximating Wald's strategy, do satisfy several key experimental constraints and reach the experimentally observed level of accuracy of *hunchback* expression within the (apparently) very stringent time limits of the early nuclear cycles.

1 Methodological setup

1.1 The decision process of the anterior *vs* posterior *hunchback* expression

The problem faced by nuclei in their decision of anterior *vs* posterior developmental fate is sketched in Fig. 1 a. We limit our investigation of promoter architectures to the six experimentally identified Bicoid binding sites (Fig. 1 b). We

do not consider the known Hunchback binding sites because before nuclear cycle 13 there is little time to produce sufficient concentrations of zygotic proteins for a significant feedback effect and the measured maternal *hunchback* profile has not been shown to alter anterior-posterior decision-making. Following the observation that Bcd readout is the leading factor in nuclei fate determination [31], we also neglect the role of other maternal gradients, e.g. Caudal, Zelda or Capicua [32, 33, 34, 8], since the readout of these morphogens can only contribute additional information and decrease the decision time. We focus on the proximal promoter since no active enhancers have been identified for the *hunchback* locus in nuclear cycles 11-13 [35]. Our results can be generalized to enhancers, the addition of which only further improves the speed-accuracy efficacy. Since our goal is to show that accurate decisions can be made rapidly, we focus on the *worst case decision-making scenario*: the positional information [36] is gathered through a readout of the Bicoid concentration only, and the decision is assumed to be made independently in each nucleus. Having additional information available and/or coupling among nuclei can only strengthen our conclusion.

The profile of the average concentration of the maternal morphogen Bicoid $L(x)$ is well represented by an exponential function that decreases from the anterior toward the posterior of the embryo : $L(x) = L_0 e^{-5(x-x_0)/100}$, where x is the position along the anterior-posterior axis measured in terms of percentage egg-length (EL), and x_0 is the position of half maximum *hb* expression corresponding to L_0 Bcd concentration. The decay length $\lambda = 5$ corresponds to 20% EL [23]. Nuclei convert the graded Bicoid gradient into a sharp border of *hunchback* expression (Fig. 1 a), with high and low expressions of the *hunchback* promoter at the left and the right of the border respectively [37, 38, 39, 12, 1, 13, 14, 40, 34, 8]. We define the *border region* of width δ_x symmetrically around x_0 by the dashed lines in Fig. 1 a. δ_x is related to the positional resolution [24, 34] of the anterior-posterior decision: it is the minimal distance measured in percentages of egg-length between two nuclei's positions, at which the nuclei can distinguish the Bcd concentrations. Although this value is not known exactly, a lower bound is estimated as $\delta_x \sim 2\%$ EL [23], which corresponds to the width of one nucleus.

We denote the Bcd concentration at the anterior (respectively posterior) boundary of the border region by L_1 (respectively L_2) (see Fig. 1 a). At each position x, nuclei compare the probability that the local concentration $L(x)$ is greater than L_1 (anterior) or smaller than L_2 (posterior). By using current best estimates of the parameters (see Appendix A), a classic fixed-time-decision integration process and an integration time of 270 seconds (the duration of the interphase in nuclear cycle 11 [34]), we compute in Fig. 1 c the probability of error per nucleus for each position in the embryo (see Appendix B for details). As expected, errors occur overwhelmingly in the vicinity of the border region, where the decision is the hardest (Fig. 1 c). For nuclei located within the border region, both anterior and posterior decisions are correct since the nuclei lie close to both regions. It follows that, although the error rate can formally be computed in this region, the errors do not describe positional resolution mistakes and do not contribute to the total error (white zone in Fig. 1 c).

In view of Fig. 1 c and to simplify further analysis we shall focus on the boundaries of the border region : each nucleus discriminates between hypothesis 1 – the Bcd concentration is $L = L_1$, and hypothesis 2 – the Bcd concentration is $L = L_2$. To achieve a positional resolution of $\delta_x = 2\%$ EL, nuclei need to be able to discriminate between differences in Bcd concentrations on the order of 10%: $|L_2 - L_1|/L \simeq 0.1$. In addition to the variation in Bcd concentration estimates that are due to biological precision, concentration estimated using many trials follows a statistical distribution. The central limit theorem suggests that this distribution is approximately Gaussian. This assumption means that the probability that the Bcd concentration estimate deviates from the actual concentration by more than the prescribed 10% positional resolution is 32% (see Section 2.1.1 for variations on the value and arguments on the error rate). In Fig. 1 d we show that the time required under a fixed-time-decision strategy for a promoter with six binding sites to estimate the Bcd concentration within the 32% Gaussian error rate [23] close to the boundary is much longer than 270 seconds, $\simeq 40$ minutes (see Appendix B for details of the calculation). The activation rule for the promoter architecture in the figure is that all binding sites need to be bound for transcription initiation.

1.2 Identifying fast decision promoter architectures

1.2.1 The promoter model

We model the *hb* promoter as six Bcd binding sites [41, 42, 43, 44] that determine the activity of the gene (Fig. 2 a). Bcd molecules bind to and unbind from each of the $i = 1, ..., 6$ sites with rates μ_i and ν_i, which are allowed to be different for each site. For simplicity, the gene can only take two states : either it is silenced (OFF) and mRNA is not produced, or the gene is activated (ON) and mRNA is produced at full speed. While models that involve different levels of polymerase loading are biologically relevant and interesting, the simplified model allows us to gain more intuition and follows the worst-case scenario logic that we discussed in section 1.1. The same remark applies for the wide variety of promoter architectures considered in previous works [45, 34]. In particular, we assume that only the number of sites that are bound matters for gene activation (and not the specific identity of the sites). Such architectures are again a subset of the range of architectures considered in [45, 34].

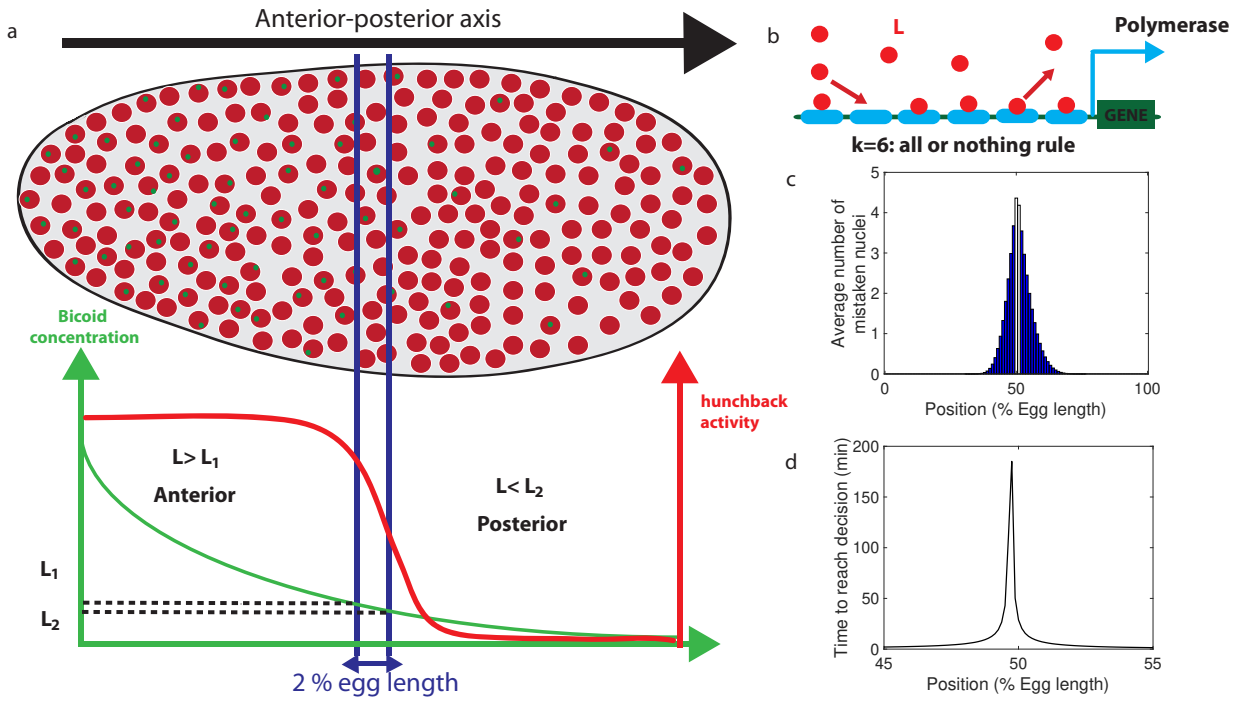

Figure 1: **Decision between anterior and posterior developmental blueprints. a.** The early *Drosophila* embryo and the Bicoid morphogen gradient. The cartoon shows a projection on one plane of the embryo at nuclear cycles 10-13, when nuclei (red dots) have migrated to the surface of the embryo [6]. The activity of the *hunchback* gene decreases along the Anterior-Posterior (AP) axis. The green dots represent active transcription loci. The average concentration $L(x)$ of maternal Bicoid decreases exponentially along the AP axis by about a factor five from the anterior (left) to the posterior (right) ends. Between the blue lines lies the boundary region. Its width δx is 2% of the egg length. *hunchback* activity decreases along the AP axis and undergoes a sharp drop around the boundary region. The half-maximum Bcd concentration position in WT embryos is shifted by about 5% of the egg-length towards the anterior with respect to the mid-embryo position [38]. We consider this *hunchback* half maximum expression as a reference point when describing the AP axis of the embryo. The *hunchback* readout defines the cell fate decision whether each nucleus will follow an anterior or the posterior gene expression program. **b.** A typical promoter structure contains six binding sites for Bicoid molecules present at concentration L. $k = 6$ indicates that the gene is active only when all binding sites are occupied, defining an all-or-nothing promoter architecture. Other forms and details of the promoter structure will be discussed in Figure 2 and Figure 3. **c.** The average number of nuclei making a mistake in the decision process as a function of the egg length position at cycle 11. For a fixed-time decision process completed within $T = 270$ seconds (and $k = 6$, i.e. all-or-nothing activation scheme), a large number of nuclei make the wrong decision (full blue bars). $T = 270$ seconds is the duration of the interphase of nuclear cycle 11 [34]. For nuclei located in the boundary region either answer is correct so that we leave these bars unfilled. Most errors happen close to the boundary, as intuitively expected. See Appendix B for a detailed description of how the error is computed for the fixed-time decision strategy. **d.** The time needed to reach the standard error probability of 32 % [23] for the same process as in panel c (see also Section 2.1.1) as a function of egg length position. Decisions are easy away from the center but the time required for an accurate decision soars close to the boundary up to 50 minutes – much longer than the embryological times. Parameters for panels **(c)** and **(d)** are 6 binding sites that bind and unbind Bicoid without cooperaivity and a diffusion limited on rate per site $\mu_{\max} L = 0.124 s^{-1}$, and an unbinding rate per site $\nu_1 = 0.0154 s^{-1}$ that lead to half activation in the boundary region.

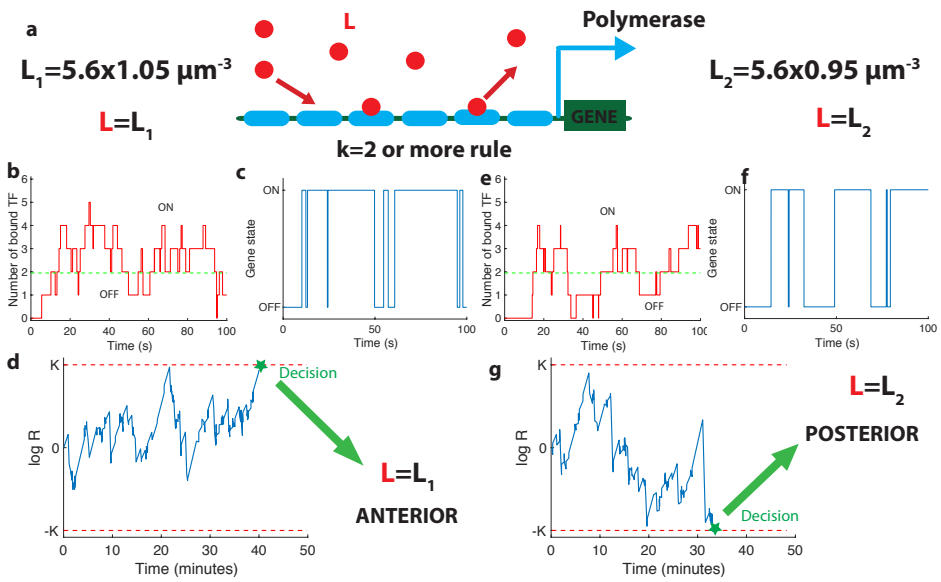

Figure 2: **The relation between promoter structure and on-the-fly decision-making. a.** Using six Bicoid binding sites, the promoter decides between two hypothetical Bcd concentrations $L = L_1$ and $L = L_2$, given the actual (unknown) concentration L in the nucleus. The number of occupied Bicoid sites fluctuates with time (**b.**) and we assume the gene is expressed (**c.**) when the number of occupied Bicoid binding sites on the promoter is $\geq k$ (green dashed line, here $k = 2$). The gene activity defines a non-Markovian telegraph process. The ratio of the likelihoods that the time trace of this telegraph process is generated by $L = L_1$ *vs* $L = L_2$ is the log-likelihood ratio used for decision-making (**d.**). The log-likelihood ratio undergoes random excursions until it reaches one of the two decision boundaries $(K, -K)$. In **d.** the actual concentration is $L = L_1$ and the log-likelihood ratio hits the upper barrier and makes the right decision. When $L = L_2$, less Bicoid binding sites are occupied (**e.**) and the gene is less likely to be expressed (**f.**), resulting in a negative drift in the log-likelihood ratio, which directs the random walk to the lower boundary $-K$ and the $L = L_2$ decision (**g.**). We consider that all six binding sites bind Bicoid independently and are identical with binding rate per site $\mu_{\max} L = 0.07 s^{-1}$ and unbinding rate per site $\nu_1 = 0.08 s^{-1}$, $e = 0.2$, $k = 2$, $L = L_1 = 5.88 \mu m^{-3}$ for panels (**b.**, **c.**, **d.**) and $L = L_2 = 5.32 \mu m^{-3}$ (**e.**, **f.**, **g.**) .

The dynamics of our model is a Markov chain with seven states with probability P_i corresponding to the number of sites occupied: from all sites unoccupied (probability P_0) to all six sites bound by Bcd molecules (probability P_6). The minimum number k of bound Bicoid sites required to activate the gene divides this chain into the two disjoint and complementary subsets of active states ($P_{\text{ON}} = \sum_{i=k}^{6} P_i$, for which the gene is activated) and inactive states ($P_{\text{OFF}} = \sum_{i=0}^{k-1} P_i$, for which the gene is silenced) as illustrated in Fig. 2 b and d.

As Bicoid ligands bind and unbind the promoter (Fig. 2 b), the gene is successively activated and silenced (Fig. 2 c). This binding/unbinding dynamics results in a series of OFF and ON activation times that constitute all the information about the Bcd concentration available to downstream processes to make a decision. We note that the idea of translating the statistics of binding-unbinding times into a decision remains the same as in the Berg-Purcell approach, where *only* the activation times are translated into a decision (and not the deactivation times). The promoter architecture determines the relationship between Bcd concentration and the statistics of the ON-OFF activation time series, which makes it a key feature of the positional information decision process. Following Ref. [27], we model the decision process as a Sequential Probability Ratio Test (SPRT) based on the time series of gene activation. At each point in time, SPRT computes the likelihood P of the observed time series under both hypotheses $P(L_1)$ and $P(L_2)$ and takes their ratio : $R(t) = P(L_1)/P(L_2)$. The logarithm of $R(t)$ undergoes stochastic changes until it reaches one of the two decision threshold boundaries K or $-K$ (symmetric boundaries are used here for simplicity) (Fig. 2 d). The decision threshold boundaries K are set by the error rate e for making the wrong decision between the hypothetical concentrations : $K = \log\left((1-e)/e\right)$ (see [27] and Appendix C.5). The choice of K or e depends on the level of reproducibility desired for the decision process. We set $K \simeq 0.75$, corresponding to the widely used error rate $e \simeq 0.32$ of being more than one standard deviation away from the mean of the estimate for the concentration assumed to be unbiased in a Gaussian

model (see Section 1.1 above). The statistics of the fluctuations in likelihood space are controlled by the values of the Bcd concentrations: when Bcd concentration is low, small numbers of Bicoid ligands bind to the promoter (Fig. 2 e) and the *hb* gene spends little time in the active expression state (Fig. 2 f), which leads to a negative drift in the process and favors the lower one of the two possible concentrations (Fig. 2 g).

1.2.2 Mean decision time : connecting drift-diffusion and Wald's approaches

In this section, we develop new methods to determine the statistics of gene switches between the OFF and ON expression states. Namely, by relating Wald's approach [26] with drift-diffusion, we establish the equality between the drift and diffusion coefficients in decision making space for difficult decision problems, i.e. when the discrimination is hard, we elucidate the reason underlying the equality. That allows us to effectively determine long-term properties of the likelihood log-ratio and compute mean decision times for complex architectures.

A gene architecture consists of N binding sites and is represented by $N+1$ Markov states corresponding to the number of bound TF, and the rates at which they bind or unbind (Fig. 3 a). For a given architecture, the dynamics of binding/unbinding events and the rules for activation define the two probability distributions $P_{\mathrm{OFF}}(t, L)$ and $P_{\mathrm{ON}}(s, L)$ for the duration of the OFF and ON times, respectively (Fig. 3b). The two series are denoted $\{t_i\}_{1\leq i\leq J^+}$ and $\{s_j\}_{1\leq j\leq J^-}$, where J^+ and J^- are the number of switching events in time t from OFF to ON and vice versa. For those cases where the two concentrations L_1 and L_2 are close and the discrimination problem is difficult (which is the case of the *Drosophila* embryo), an accurate decision requires sampling over many activation and deactivation events to achieve discrimination. The logarithm of the ratio $R(t)$ can then be approximated by a drift–diffusion equation: $d\log R(t)/dt = V + \sqrt{2D}\eta$, where V is the constant drift, i.e. the bias in favor of one of the two hypotheses, D is the diffusion constant and η a standard Gaussian white noise with zero mean and delta-correlated in time [26, 27]. The decision time for the case of symmetric boundaries $K = -K_- = K_+$, is given by the mean first-passage time for this biased random walk in the log-likelihood space [46, 27]:

$$\langle T\rangle = \frac{K\tanh(VK/2D)}{V}\,. \tag{1}$$

Note that in this approximation all the details of the promoter architecture are subsumed into the specific forms of the drift V and the diffusion D.

Drift. We assume for simplicity that the time series of OFF and ON times are independent variables (when this assumption is relaxed, see Appendix G). This assumption is in particular always true when gene activation only depends on the number of bound Bicoid molecules. Under these assumptions we can apply Wald's equality [47, 48] to the log-likelihood ratio, $\log R(t)$. Wald considered the sum of a random number M of independent and identically distributed (i.i.d.) variables. The equality that he derived states that if M is independent of the outcome of variables with higher indices $(X_i)_{i>M}$ (i.e. M is a stopping time), then the average of the sum is the product $\langle M\rangle\,\langle X_i\rangle$.

Wald's equality applies to our likelihood sum ($\sum_i^M \log R_i$ of the likelihoods, where M is the number of ON and OFF times before a given (large) time t). We conclude the drift of the log-likelihood ratio, $\log R(t)$, is inversely proportional to $(\tau_{\mathrm{ON}} + \tau_{\mathrm{OFF}})$, where τ_{ON} is the mean of the distribution of ON times $P_{\mathrm{ON}}(t, L)$ and τ_{OFF} is the mean of the distribution of OFF times $P_{\mathrm{OFF}}(s, L)$. The term $(\tau_{\mathrm{ON}} + \tau_{\mathrm{OFF}})$ determines the average speed at which the system completes an activation/deactivation cycle, while the average $\langle\log R_i\rangle$ describes how much deterministic bias the system acquires on average per activation/deactivation cycle. The latter can be re-expressed in terms of the Kullback-Leibler divergence $D_{KL}(f||g) = \int_0^\infty dt' f(t')\log\left(f(t')/g(t')\right)$ between the distributions of the OFF and ON times calculated for the actual concentration L and each one of the two hypotheses, L_1 and L_2 :

$$\begin{aligned} V = \frac{1}{(\tau_{\mathrm{ON}} + \tau_{\mathrm{OFF}})}\big[&D_{KL}(P_{\mathrm{OFF}}(.,L)||P_{\mathrm{OFF}}(.,L_2)) - D_{KL}(P_{\mathrm{OFF}}(.,L)||P_{\mathrm{OFF}}(.,L_1)) \\ &+ D_{KL}(P_{\mathrm{ON}}(.,L)||P_{\mathrm{ON}}(.,L_2)) - D_{KL}(P_{\mathrm{ON}}(.,L)||P_{\mathrm{ON}}(.,L_1))\big]\,. \end{aligned} \tag{2}$$

Eq. 2 quantifies the intuition that the drift favors the hypothetical concentration with the time distribution which is the closest to that of the real concentration L (Fig. 3 b).

Diffusivity : Why it is more involved to calculate and how we circumvent it. While the drift has the closed simple form in Eq. 2, the diffusion term is not immediately expressed as an integral. The qualitative reason is as follows. Computing the likelihood of the two hypotheses requires computing a sum where the addends are stochastic (ratios of likelihoods) and the number of terms is also stochastic (the number of switching events). These two random variables are correlated: if the number of switching events is large, then the times are short and the likelihood is probably higher for large concentrations. While the drift is linear in the above sum (so that the average of the sum can be treated as shown above), the diffusivity depends on the square of the sum. The diffusivity involves then the correlation of

times and ratios [49], which is harder to obtain as it depends *a priori* on the details of the binding site model (see Appendices C.5 and C.7 for details).

We circumvent the calculation of the diffusivity by noting that the same methods used to derive Eq. (1) also yield the probability of first absorption at one of the two boundaries, say $+K$ (see Appendix C.5) :

$$\Pi_K = \frac{e^{VK/D}}{1 + e^{\frac{KV}{D}}} \,. \tag{3}$$

By imposing $\Pi_K = 1 - e$, we obtain $VK/D = \log\left((1-e)/e\right)$ and the comparison with the expression of $K = \log\left((1-e)/e\right)$ leads to the equality $D = V$.

The above equality is expected to hold for difficult decisions only. Indeed, drift-diffusion is based on the continuity of the log-likelihood process and Wald's arguments assume the absence of substantial jumps in the log-likelihood over a cycle. In other words, the two approaches overlap if the hypotheses to be discriminated are close. For very distinct hypotheses (easy discrimination problems) the two approaches may differ from the actual discrete process of decision and among themselves. We expect then that $V = D$ holds only for hypotheses that are close enough, which is verified by explicit examples (see Appendix C.5). The Appendix also verifies $V = D$ by expanding the general expression of V and D for close hypotheses. The origin of the equality is discussed below.

Using $V = D$, we can reduce the general formula Eq. (1) to

$$\langle T \rangle = \frac{K \tanh(K/2)}{V} = \frac{K}{V}\left(1 - 2e\right) \,, \tag{4}$$

which is formula 4.8 in [26] and it is the expression that we shall be using (unless stated otherwise) in the remainder of the paper.

The additional consequence of the equality $V = D$ is that the argument $VK/2D$ of the hyperbolic tangent in Eq. (1) is $\simeq K/2 = \ln\left(\sqrt{(1-e)/e}\right)$. It follows that for any problem where the error $e \ll 1$, the argument of the hyperbolic tangent is large and the decision time is weakly dependent on deviations to $V = D$ that occur when the two hypotheses differ substantially. A concrete illustration is provided in Appendix C.6.

Single binding site example. As an example of the above equations, we consider the simplest possible architecture with a single binding site ($N = 1$), where the gene activation and de-activation processes are Markovian. In this case the de-activation rate ν is independent of TF concentration and the activation rate is exponentially distributed $P_{\rm OFF}(L,t) = kLe^{kLt}$. We can explicitly calculate the drift $V = \nu kL/(\nu + kL)(\log(L_1/L_2) + (L_2 - L_1)/L)$ (Eq. 2) and expand it for $L_2 = L$ and $L_1 = L + \delta L$, at leading order in δL. Inserting the resulting expression into Eq. 4, we conclude that

$$\langle T \rangle = \frac{\nu + kL}{\nu kL}\frac{2KL^2}{\delta L^2}\tanh\left(\frac{K}{2}\right), \tag{5}$$

decreases with increasing relative TF concentration difference $\delta L/L$ and gives a very good approximation of the complete formula (see SI Fig 9 a-c with different values of $\delta L/L$).

Eqs. 2 and 4 greatly reduce the complexity of evaluating the performance of architectures, especially when the number of binding sites is large. Alternatively, computing the correlation of times and log-likelihoods would be increasingly demanding as the size of the gene architecture transfer matrices increase. As an illustration, Fig. 3 compares the performance of different activation strategies : the 2-or-more rule ($k = 2$), which requires at least two Bcd binding sites to be occupied for *hb* promoter activation (Fig. 3a-d in blue), and the 4-or-more rule ($k = 4$) (Fig. 3a-d in red) for fixed binding and unbinding parameters. Fig. 3c shows that stronger drifts lead to faster decisions. The full decision time probability distribution is computed from the explicit formula for its Laplace transform [27] (Fig. 3d). With the rates chosen for Fig. 3, the $k = 4$ rule leads to an ON time distribution that varies strongly with the concentration, making it easier to discriminate between similar concentrations: it results in a stronger average drift that leads to a faster decision than $k = 2$ (Fig. 3 d).

What is the origin of the $V = D$ equality? The special feature of the SPRT random process is that it pertains to a log-likelihood. This is at the core of the $V = D$ equality that we found above. First, note that the equality is dimensionally correct because log-likelihoods have no physical dimensions so that both V and D have units of $time^{-1}$. Second, and more important, log-likelihoods are built by Bayesian updating, which constrains their possible variations. In particular, given the current likelihoods $P_1(t) = \Pi_j P_{\rm ON}(t_j, L_1)P_{\rm OFF}(s_j, L_1)$ and $P_2(t) = \Pi_j P_{\rm ON}(t_j, L_2)P_{\rm OFF}(s_j, L_2)$ at time t for the two concentrations L_1 and L_2 and the respective probabilities $Q_1(t) = P_1/(P_1 + P_2)$ and $Q_2(t) = 1 - Q_1$ of the two hypotheses, it must be true that the expected values after a certain time Δt remain the same if the expectation

is taken with respect to the current $P_i(t)$ (see, e.g. [50]). In formulae, this implies that the average variation of the probability Q_2 over a given time Δt that is

$$\langle \Delta Q_2 \rangle = Q_1 \langle \Delta Q_2 \rangle_1 + Q_2 \langle \Delta Q_2 \rangle_2 \,, \tag{6}$$

should vanish (see Appendix C.5 for a derivation). Here, $\langle \Delta Q_2 \rangle_1$ is the expected variation of Q_2 under the assumption that hypothesis 1 is true and $\langle \Delta Q_2 \rangle_2$ is the same quantity but under the assumption that hypothesis 2 is true. We notice now that $Q_2(t) = \frac{1}{1+e^{\mathcal{L}(t)}}$, where $\mathcal{L} = \log R$ is the log-likelihood, and that the drift-diffusion of the log-likelihood implies that $\langle \Delta \mathcal{L} \rangle_1 = V \Delta t$, $\langle \Delta \mathcal{L} \rangle_2 = -V \Delta t$ and $\langle (\Delta \mathcal{L} - \langle \Delta \mathcal{L} \rangle_1)^2 \rangle_1 = \langle (\Delta \mathcal{L} - \langle \Delta \mathcal{L} \rangle_2)^2 \rangle_2 = 2D\Delta t$. By using that $dQ_2/d\mathcal{L} = -Q_1 Q_2$ and $d^2 Q_2/d\mathcal{L}^2 = -Q_1 Q_2 (Q_2 - Q_1)$, we finally obtain that

$$\langle \Delta Q_2 \rangle = Q_1 Q_2 \left(Q_2 - Q_1 \right) \Delta t \left[V - D \right] \,, \tag{7}$$

and imposing $\langle \Delta Q_2 \rangle = 0$ yields the equality $V = D$. Note that the above derivation holds only for close hypotheses, otherwise the velocity and the diffusivity under the two hypotheses do not coincide.

1.2.3 Additional embryological constraints on promoter architectures

In addition to the requirements imposed by their performance in the decision process (green dashed line in Fig. 4a), promoter architectures are constrained by experimental observations and properties that limit the space of viable promoter candidates for the fly embryo. A discussion about their possible function and their relation to downstream decoding processes is deferred to the final section.

First, we require that the average probability for a nucleus to be active in the boundary region is equal to 0.5, as it is experimentally observed [40] (Fig. 1a). This requirement mainly impacts and constrains the ratio between binding rates μ_i and unbinding rates ν_i.

Second, there is no experimental evidence for active search mechanisms of Bicoid molecules for its targets. It follows that, even in the best case scenario of a Bcd ligand in the vicinity of the promoter always binding to the target, the binding rate is equal to the diffusion limited arrival rate $\mu_{\max} L \simeq 0.124 s^{-1}$ (Appendix A). As a result, the binding rates μ_i are limited by diffusion arrivals and the number of available binding sites: $\mu_i \leq \mu_{\max}(7-i)$ (black dashed line in Fig. 4b), where L is the concentration of Bicoid. This sets the timescale for binding events. In Appendix A, we explore the different measured values and estimates of parameters defining the diffusion limit $\mu_{\max} L$ and their influence on the decision time (see Table 1 for all the predictions).

Third, as shown in Fig. 1, the *hunchback* response is sharp, as quantified by fitting a Hill function to the expression level *vs* position along the egg length. Specifically, the *hunchback* expression (in arbitrary units) $f_{\rm hb}$ is well approximated as a function of the Bicoid concentration $L(x)$ by the Hill function $f_{\rm hb}(x) \simeq L(x)^H / (L(x)^H + L_0^H)$, where L_0 is the Bcd concentration at the half-maximum hb expression point and H is the Hill coefficient (Fig. 1a). Experimentally, the measured Hill coefficient for mRNA expression from the WT *hb* promoter is $H \sim 7-8$ [8, 34]. Recent work [34] suggests that these high values might not be achieved by Bicoid binding sites only. Given current parameter estimates and an equilibrium binding model, [34] shows that a Hill coefficient of 7 is not achievable within the duration of an early nuclear cycle ($\simeq 5$ min). That points at the contribution of other mechanisms to pattern steepness. Given these reasons (and the fact that we limit ourselves only to a model with 6 equilibrium Bcd binding sites only), we shall explore the space of possible equilibrium promoter architectures limiting the steepness of our profiles to Hill coefficients $H \sim 4-5$.

1.2.4 Numerical procedure for identifying fast decision-making architectures

Using Eqs. 2 and 4, we explore possible *hb* promoter architectures and activation rules to find the ones that minimize the time required for an accurate decision, given the constraints listed in Section 1.2.3. We optimize over all possible binding rates $(\mu_i)_{1 \leq i \leq 6}$ (μ_1 is the binding rate of the first Bcd ligand and μ_6 the binding rate of the last Bcd ligand when 5 Bcd ligands are already bound to the promoter), and the unbinding rates $(\nu_i)_{1 \leq i \leq 6}$ (ν_1 is the unbinding rate of a single Bcd ligand bound to the promoter and ν_6 is the unbinding rate of all Bcd ligands when all six Bcd binding sites are occupied). We also explore different activation rules by varying the minimal number of Bcd ligands k required for activation in the k-or-more activation rule [45, 34]. We use the most recent estimates of biological constants for the *hb* promoter and Bcd diffusion (see Appendix A) and set the error rate at the border to 32%[12, 15]. Reasons for this choice were given in subsection 1.1 and will be revisited in subsection 2.1.1, where we shall introduce some embryological considerations on the number of nuclei involved in the decision process and determine the error probability accordingly. The optimization procedure that minimized the average decision time for different values of k and H is implemented using a mixed strategy of multiple random starting points and steepest gradient descent (Fig. 4a).

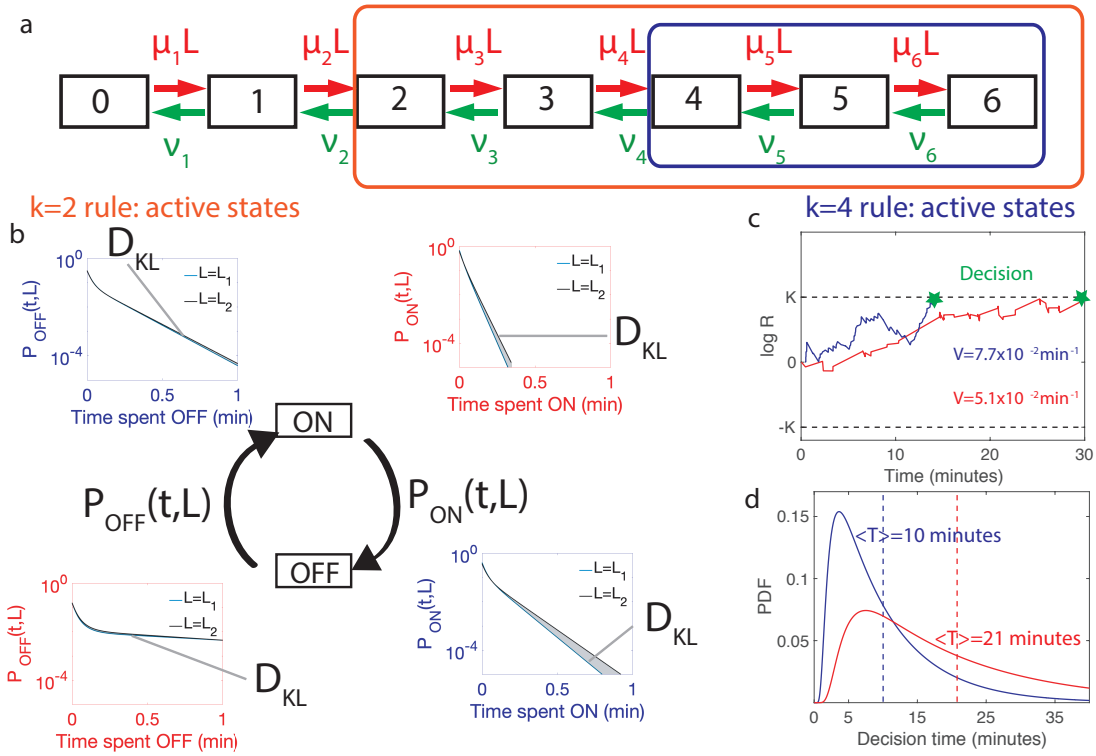

Figure 3: **Comparing the performance of two promoter activation rules. a.** The dynamics of the six Bcd binding site promoter is represented by a 7 state Markov chain where the state number indicates the number of occupied Bicoid binding sites. The boxes indicate the states n which the gene is expressed for the 2-or-more activation rule (red box and red in panels **b.**- **d.**) where the gene is active when 2-or-more TF are bound and the 4-or-more activation rule (blue box and blue in panels **b.**- **d.**) where the gene is active when 4-or-more TF are bound. **b.** The dynamics of TF binding translates into bursting and inactive periods of gene activity. The OFF and ON time distributions are different for the two hypothetical concentrations (blue boxes for $k = 4$ and red boxes for $k = 2$). The Kullback-Leibler divergence between the distributions for the two hypothetical concentrations (D_{KL}) sets the decision time and is related to the difference in the area below the two distributions. For the $k = 4$ activation rule, the OFF time distributions are similar for the two hypothetical concentrations but the ON times distributions are very different. The ON times are more informative for the $k = 4$ activation rule than the $k = 2$ activation rule **c.** The drift V of the log-likelihood ratio characterizes the deterministic bias in the decision process. The differences in **b.** translate into larger drift for $k = 4$ for the same binding/unbinding dynamics. **d.** The distribution of decision times (calculated as the first-passage time of the log-likelihood random walk) decays exponentially for long times. Higher drift leads to on average faster decisions than for the $k = 4$ activation rule (mean decision times are shown in dashed lines). For all panels the six binding sites are independent and identical with $L = L_1 = 5.88\ \mu m^{-3}$, $L_2 = 5.32\ \mu m^{-3}$, $e = 0.1$, $\mu_{\max} L = 0.14\ s^{-1}$ and $\nu = 0.08\ s^{-1}$ for all binding sites.

2 Results

2.1 Logic and properties of the identified fast decision architectures

The main conclusion we reach using the methodology presented in section 1 is that there exist promoter architectures that reach the required precision within a few minutes and satisfy all the additional embryological constraints that were discussed previously (Fig. 4a). The fastest promoters (blue crosses in Fig. 4a) reach a decision within the time of nuclear cycle 11 (green line in Fig. 4a) for a wide range of activation rules. Even imposing steep readouts ($H > 4$) allows us to identify relatively fast promoters, although imposing the nuclear cycle time limit, pushes the activation rule to smaller k. The optimal architectures differ mainly by the distribution of their unbinding rates (Fig. 4b). We shall now discuss their properties, namely the binding times of Bicoid molecules to the DNA binding sites, and the dependence of the promoter activity on various features, such as activation rules and the number of binding sites in detail. Together, these results elucidate the logic underlying the process of fast decision-making.

2.1.1 How many nuclei make a mistake?

The precision of a stochastic readout process is defined by two parameters: the resolution of the readout δx, and the probability of error, which sets the reproducibility of the readout. In Fig. 4 we have used the statistical Gaussian error level (32%) to obtain our results. However, the error level sets a crucial quantity for a developing organism and it is important to connect it with the embryological process, namely how many nuclei across the embryo will fail to properly decide (whether they are positioned in the anterior or in the posterior part of the embryo). To make this connection, we compute this number for a given average decision time T and we integrate the error probability along the AP axis to obtain the error per nucleus e_s. The expected number of nuclei that fail to correctly identify their position is given by $\langle n_{\rm error}\rangle = e_s 2^{c-1}$, where c is the nuclear cycle and we have neglected the loss due to yolk nuclei remaining in the bulk and arresting their divisions after cycle 10 [51]. Assuming a 270s readout time – the total interphase time of nuclear cycle 11 ([34]) – for the fastest architecture identified above and an error rate of 32%, we find that $\langle n_{\rm error}\rangle \simeq 0.3$, that is an essentially fail-proof mechanism. This number can be compared with > 30 nuclei in the embryo that make an error in a $\langle T\rangle = 270$s read-out in a Berg-Purcell-like fixed time scheme (integrated blue area in Fig. 1c).

Conversely, for a given architecture, reducing the error level increases drastically the mean first-passage time to decision: the mean time for decision as a function of the error rate for the fastest architecture identified with $H > 5$ and $k = 1$ is shown in Fig. 7. The decision can be made in about a minute for $e = 32\%$ but requires on average 10 minutes for $e = 10\%$ (Fig. 7). Note that, because the mean first-passage depends simply on the inverse of the drift per cycle (Eq. 4), the relative performance of two architectures is the same for any error rate so that the fastest architectures identified in Fig. 4a are valid for all error levels.

2.1.2 Residence times among the various states

As shown in Ref. [34], high Hill coefficients in the *hunchback* response are associated with frequent visits of the extreme expression states where available binding sites are either all empty (state 0), or all occupied (state 6). Fig. 4c provides a concrete illustration by showing the distribution of residence times for the promoter architectures that yield the fastest decision times for $k = 3$ and no constraints (blue bars), $H > 4$ (red bars) and $H > 5$ (black bars). When there are no constraints on the slope of the *hunchback* response, the most frequently occupied states are close to the ON-OFF transition (2 and 3 occupied binding sites in Fig. 4c) to allow for fast back and forth between the active and inactive states of the gene and thereby gather information more rapidly by reducing $\tau_{\rm ON} + \tau_{\rm OFF}$ (see formulae 2 and 4).

We notice that for higher Hill coefficients, the system transits quickly through the central states (in particular states with 3 and 4 occupied Bcd sites, Fig. 4 red and black bars). As expected for high Hill coefficients, such dynamics requires high cooperativity. Cooperativity helps the recruitment of extra transcription factors once one or two of them are already bound and thus speeds up the transitioning through the states with 2, 3 and 4 occupied binding sites. An even higher level of cooperativity is required to make TF DNA binding more stable when 5 or 6 of them are bound, reducing the OFF rates ν_5 or ν_6 (Fig. 4b).

2.1.3 The (short) binding times of Bicoid on DNA

The distribution of times spent bound to DNA of individual Bicoid molecules is shown in Fig. 4d obtained from Monte Carlo simulations using rates from the fastest architecture with $H > 5$ and $k = 2$. We find an exponential decay, an average bound time of about 7.1s and a median around 0.5s. Our median-time-bound prediction is of the same order of magnitude as the observed bound times seen in recent experiments by Mir et al [52], who found short (mean ~ 0.629s and median ~ 0.436s based on exponential fits), yet quite distinguishable from background, bound times to DNA. These results were considered surprising because it seemed unclear how such short binding events could be consistent

with the processing of ON and OFF gene switching events. Our results show that such short binding times may actually be instrumental in achieving the tradeoff between accuracy and speed, and rationalize how longer activation events are still achieved despite the fast binding and unbinding. High cooperativity architectures lead to non-exponential bound times to DNA (Fig. 4d) for which the typical bound time (median) is short but the tail of the distribution includes slower dynamics that can explain longer activation events (the mean is much larger than the median). This result suggests that cells can use the bursty nature of promoter architectures to better discriminate between TF concentrations.

In Ref. [52], the raw distribution comprises both non-specific and specific binding and cannot be directly compared to simulation results. Instead, we use the largest of the two exponents fit for the boundary region [52], which should correspond to specific binding. The agreement between the distributions in Fig. 4d is overall good, and we ascribe discrepancies to the fact that Mir et al. [52] fit two exponential distributions assuming the observed times were the convolution of exponential specific and non-specific binding times. Yet the true specific binding time distribution is likely not exponential, e.g. due to the effect of binding sites having different binding affinities. We show in Supplementary Fig. 13 that the two distributions are very similar and hard to distinguish once they are mixed with the non-specific part of the distribution.

2.1.4 Activation rules

In the parameter range of the early fly embryo, the fastest decision-making architectures share the 1-or-more ($k = 1$) activation rule : the promoter switches rapidly between the ON and OFF expression states and the extra binding sites are used for increasing the size of the target rather than building a more complex signal. Architectures with $k = 2$ and $k = 3$ activation rules can make decisions in less than 270 seconds and satisfy all the required biological constraints. Generally speaking, our analysis predicts that fast decisions require a small number of Bicoid binding sites (less than three) to be occupied for the gene to be active. The advantage of the $k = 2$ or $k = 3$ activation rules is that the ON and OFF times are on average longer than for $k = 1$, which makes the downstream processing of the readout easier. We do not find any architecture satisfying all the conditions for the $k = 4, 5, 6$ activation rules, although we cannot exclude there could be some architectures outside of the subset that we managed to sample, especially for the $k = 4$ activation rules where we did identify some promoter structures that are close to the time constraint.

Activation rules with higher k can give higher information per cycle for the ON rate, yet they do not seem to lead to faster decisions because of the much longer duration of the cycles. To gain insight on how the tradeoff between fast cycles and information affects the efficiency of activation rules, we consider architectures with only two binding sites, which lend to analytical understanding (Fig. 5 a and b). Both of these considered architectures are out of equilibrium and require energy consumption (as opposed to the two equilibrium architectures of Fig. 5 c and d).

When is 1-or-more faster than all-or-nothing activation? A first model has the promoter consisting of two binding sites with the all-or-nothing rule $k = 2$ (Fig. 5 a). We consider the mathematically simpler, although biologically more demanding, situation where TFs cannot unbind independently from the intermediate states – once one TF binds, all the binding sites need to be occupied before the promoter is freed by the unbinding with rate ν of the entire complex of TFs. This situation can be formulated in terms of a non-equilibrium cycle model, depicted for two binding sites in Fig. 5 a. The activation time is a convolution of the exponential distributions $P_{\rm OFF}(t, L) = \frac{\mu_1\mu_2 L}{\mu_2-\mu_1}\left(e^{-\mu_1 Lt} - e^{-\mu_2 Lt}\right)$. In the simple case when the two binding rates are similar ($\mu_1 \simeq \mu_2$), the OFF times follow a Gamma distribution and the drift and diffusion can be computed analytically (see Appendix D). When the two binding rates are not similar the drift and diffusion must be obtained by numerical integration (see Appendix D).

In the first model described above (Fig. 5 a), deactivation times are independent of the concentration and do not contribute to the information gained per cycle and, as a result, to $V/(\tau_{\rm ON} + \tau_{\rm OFF})$. To explore the effect of deactivation time statistics on decision times, we consider a cycle model where the gene is activated by the binding of the first TF (the 1-or-more $k = 1$ rule) and deactivation occurs by complete unbinding of the TFs complex (Fig. 5 b). The resulting activation times are exponentially distributed and contribute to drift and diffusion as in the simple two state promoter model (Fig. 5 d). The deactivation times are a convolution of the concentration-dependent second binding and the concentration-independent unbinding of the complex and their probability distribution is $P_{\rm ON}(t, L) = \frac{\nu\mu_2 L}{\nu-\mu_2 L}\left(e^{-\mu_2 Lt} - e^{-\nu t}\right)$. Drift and diffusion can be obtained analytically (Appendix D). The concentration-dependent deactivation times prove informative for reducing the mean decision time at low TF concentrations but increase the decision time at high TF concentrations compared to the simplest irreversible binding model. In the limit of unbinding times of the complex ($1/\nu$) much larger than the second binding time ($1/\mu_2 L$), no information is gained from deactivation times. In the limit of $\mu_1 L/\nu \to \infty$, the $k = 1$ model reduces to a one binding site exponential model and the two architectures (Fig. 5 b and d) have the same asymptotic performance.

Within the irreversible schemes of Fig. 5 a and Fig. 5 b, the average time of one activation/deactivation cycle is the same for the all-or-nothing $k = 2$ and 1-or-more $k = 1$ activation schemes. The difference in the schemes comes from

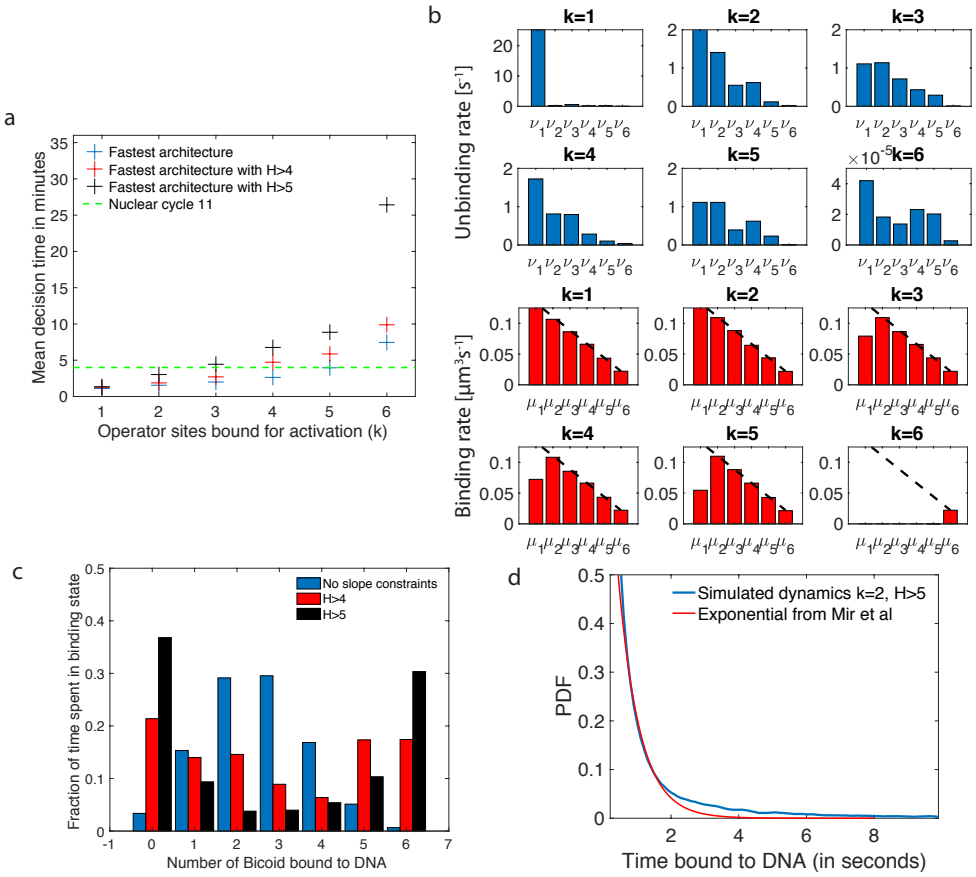

Figure 4: **Performance, constraints and statistics of fastest decision-making architectures. a.** Mean decision time for discriminating between two concentrations with $|L_2 - L_1| = 0.1L$ and $e = 0.32$. Results shown for the fastest decision-making architectures for different activation rules and steepness constraints. For a given activation rule (k), we optimize over all values of ON rates μ_i and OFF rates ν_i (see Fig. 3 a) within the diffusion limit ($0.124\ s^{-1}$ per site), constraining the steepness H and probability of nuclei to be active at the boundary (see section 1.2.3). The green lines denotes the interphase duration of nuclear cycle 11 and even for the strongest constraints ($H > 5$) we identify architectures that make an accurate decision within this time limit. **b.** The unbinding rates (blue) and binding rates (red) of the fastest decision-making architectures with $H > 5$ – all of these regulatory systems require cooperativity in TF binding to the promoter binding sites. The dashed line on the ON rates plots shows the upper bound set by the diffusion limit. **c.** Histogram of the probability distribution of the time spent in different Bcd binding site occupancy states for the fastest decision-making architecture for $k = 3$ and no constraints on the slope (blue), $H > 4$ (red) and $H > 5$ (black). **d.** Probability distribution of the time spent bound to th DNA by Bicoid molecules for the fastest decision-making architecture with $H > 5$ and $k = 2$. Our prediction is compared to the exponential distribution with parameters fit by Mir et al. (Ref. [52]), for the specific binding at the boundary. While the distributions are close, our simulated distribution is not exponential, as expected for the 6-binding site architecture. The non-exponential behavior in the experimental curve is likely masked by the convolution with non-specific binding. We use the boundary region concentration $L = 5.6\ \mu m^{-3}$ (see panel b, $k = 2$ for rates).

the information gained in the drift term $V/(\tau_{\mathrm{ON}} + \tau_{\mathrm{OFF}})$, which begs the question : is it more efficient to deconvolve the second binding event from the first one within the all-or-nothing $k = 2$ activation scheme, or from the deactivation event in the $k = 1$ activation scheme?

In general, the convolution of two concentration-dependent events is less informative than two equivalent independent events, and more informative than a single binding event. For small concentrations L, activation events are much longer than deactivation events. In the $k = 1$ scheme, OFF times are dominated by the concentration-dependent step $\mu_2 L$ and the two activation events can be read independently. This regime of parameters favors the $k = 1$ rule (Fig.5 e). However, when the concentration L is very large the two binding events happen very fast and for $\mu_2 L >> \nu$, in the $k = 1$ scheme, it is hard to disentangle the binding and the unbinding events. The information gained in the second binding event goes to 0 as $L \to \infty$ and the 1-or-more $k = 1$ activation scheme (Fig.5 b) effectively becomes equivalent to a single binding site promoter (Fig.5 d), making the all-or-nothing $k = 2$ activation (Fig.5 a) scheme more informative (Fig.5 e). The fastest decision time architecture systematically convolves the second binding event with the slowest of the other reactions (Fig.5 e), with the transition between the two activation schemes when the other reactions have exactly equal rates ($\mu_1 L = \nu$ line in Fig. 5 e) (see Appendix E for a derivation).

2.1.5 How the number of binding sites affects decisions

The above results have been obtained with six binding sites. Motivated by the possibility of building synthetic promoters [53] or the existence of yet undiscovered binding sites, we investigate here the role of the number of binding sites. Our results suggest that the main effect of additional binding sites in the fly embryo is to increase the size of the target (and possibly to allow for higher cooperativity and Hill coefficients). To better understand the influence of the number of binding sites on performance at the diffusion limit, we compare a model with one binding site (Fig. 5 d) to a reversible model with two binding sites where the gene is activated only when both binding sites are bound (all-or-nothing $k = 2$, Fig. 5 c). Just like for the 6 binding site architectures, we describe this two binding site reversible model by using the transition matrix of the $N + 1$ Markov chain and calculate the total activation time $P_{\mathrm{OFF}}(t, L)$.

For fixed values of the real concentration L, the two hypothetical concentrations L_1 and L_2, the error e and the second off-rate ν_2, we optimize the remaining parameters μ_1, μ_2 and ν_1 for the shortest average decision time.

For high gene deactivation rates ν_2, the fastest decision time is achieved by a promoter with one binding site (Fig. 5 f): once one ligand has bound, the promoter never goes back to being completely unbound (ν_1^*=0 in Fig. 5 c) but toggles between one and two bound TF (Fig. 5 d with $\nu = \nu_2$ and $\mu = \mu_2$). For lower values of gene deactivation rates ν_2, there is a sharp transition to a minimal $\langle T \rangle$ solution using both binding sites. In the all-or-nothing activation scheme that is used here, the distribution of deactivation times is ligand independent and the concentration is measured only through the distribution of activation times, which is the convolution of the distributions of times spent in the 0 and 1 states before activation in the 2 state. For very small deactivation ν_2 rates, it is more informative to "measure" the ligand concentration by accumulating two binding events every time the gene has to go through the slow step of deactivating (Fig. 5 c). However, for large deactivation rates little time is "lost" in the uninformative expressing state and there is no need to try and deconvolve the binding events but rather use direct independent activation/deactivation statistics from a single binding site promoter (Fig. 5 d, see Appendix F for a more detailed calculation).

2.1.6 The role of weak binding sites

An important observation about the strength of the binding sites that emerge from our search is that the binding rates are often below the diffusion limit $\mu_{\max} L_0 \simeq 0.124 s^{-1}$ (see black dashed line in Fig. 4b) : some of the ligands reach the receptor, they could potentially bind but the decision time decreases if they do not. In other words, binding sites are "weak" and, since this is also a feature of many experimental promoters [54], the purpose of this section is to investigate the rationale for this observation by using the models described in Fig. 5.

Naïvely, it would seem that increasing the binding rate can only increase the quality of the readout. This statement is only true in certain parameter regimes, and weaker binding sites can be advantageous for a fast and precise readout. To provide concrete examples, we fix the deactivation rate ν and the first binding rate μ_1 in the 1-or-more irreversible binding model of Fig. 5 b and we look for the unbinding rate μ_2^* that leads to the fastest decision. We consider a situation where the two binding sites are not interchangeable and binding must happen in a specific order. In this case, the diffusion limit states that $\mu_2 \leq \mu_1$ if the first binding is strong and happens at the diffusion limit. We optimize the mean decision time for $0 \leq \mu_2 \leq \mu_1$ (see Fig. 14 for an example) and find a range of parameters where the fastest-decision value $\mu_2^* < \mu_1$ is not as fast as parameter range allows (Fig. 5g). We note that this weaker binding site that results in fast decision times can only exist within a promoter structure that features cooperativity. In this specific case, the first binding site needs to be occupied for the second one to be available. If the two binding sites are independent, then the diffusion limit is $\mu_2 \leq \mu_1$ and the fastest $\langle T \rangle$ solution always has the fastest possible binding rates.

2.2 Predictions for Bicoid binding sites mutants

In addition to results for wild type embryos, our approach also yields predictions that could be tested experimentally by using synthetic *hb* promoters with a variable numbers of Bicoid binding sites (Fig. 6 a). For any of the fast decision-making architectures identified and activation rules chosen, we can compute the effects of reducing the number of binding sites. Specifically, our predictions for the $k = 3$ activation rule and $H > 4$ in Fig. 6 b can be compared to FISH or fluorescent live imaging measurements of the fraction of active loci at a given position along the anterior-posterior axis. Bcd binding site mutants of the WT promoter have been measured by immunostaining in cycle 14 [53] although mRNA experiments in earlier cell cycles of well characterized mutants are needed to provide for a more quantitative comparison.

An important consideration for the comparison to experimental data is that there is *a priori* no reason for the *hb* promoter to have an *optimal* architecture. We do find indeed many architectures that satisfy all the experimental constraints and are not the fastest decision-making but "good enough" *hb* promoters. A relevant question then is whether or not similarity in performance is associated with similarity in the microscopic architecture. This point is addressed in Fig. 6c, where we compare the fraction of active loci along the AP axis using several constraint-conforming architectures for $H > 4$ and the $k = 2$ and $k = 3$ activation rules. The plot shows that solutions corresponding to the same activation rule are clustered together and quite distinguishable from the rest. This result suggests that the precise values of the binding and unbinding constants are not important for satisfying the constraints, that many solutions are possible, and that FISH or MS2 imaging experiments can be used to distinguish between different activation rules. The fraction of active loci in the boundary region is an even simpler variable that can differentiate between different activation rules (Fig. 6d). Lastly, we make a prediction for the displacement of the anterior-posterior boundary in mutants, showing that a reduced numbers of Bcd sites results in a strong anterior displacement of the *hb* expression border compared to 6 binding sites, regardless of the activation rule (Fig. 6e). Error bars in Fig. 6e, that correspond to different close-to-fastest architectures, confirm that these share similar properties and different activation rules are distinguishable.

3 Discussion

The issue of precision in the Bicoid readout by the *hunchback* promoter has a long history [55, 56]. Recent interest was sparked by the argument that the amount of information at the *hunchback* locus available during one nuclear cycle is too small for the observed 2% EL distance between neighbouring nuclei that are able to make reproducible distinct decisions [12]. By using updated estimates of the biophysical parameters [13, 34], and the Berg-Purcell error estimation, we confirm that establishing a boundary with 2% variability between neighbouring nuclei would take at least about 13.4 minutes – roughly the non-transient expression time in nuclear cycle 14 [8, 34] (Appendix A). This holds for a single Bicoid binding site. An intuitive way to achieve a speed up is to increase the number of binding sites: multiple occupancy time traces are thereby made available, which provides *a priori* more information on the Bicoid concentration.

Possible advantages of multiple sites are not so easy to exploit, though. First, the various sites are close and their respective bindings are correlated [19], so that their respective occupancy time traces are not independent. That reduces the gain in the amount of information. Second, if the activation of gene expression requires the joint binding of multiple sites, the transition to the active configuration takes time. The overall process may therefore be slowed down with respect to a single binding site model, in spite of the additional information. Third, and most importantly, information is conveyed downstream via the expression level of the gene, which is again a single time trace. This channeling of the multiple sites' occupancy traces into the single time trace of gene expression makes gene activation a real information bottleneck for concentration readout. All these factors can combine and even lead to an increase in the decision time. To wit, an all-or-nothing equilibrium activation model with six identical binding sites functioning at the diffusion limit and no cooperativity takes about 38 minutes to achieve the same above accuracy. In sum, the binding site kinetics and the gene activation rules are essential to harness the potential advantage of multiple binding sites.

Our work addresses the question of which multisite promoters architecture minimize the effects of the activation bottleneck. Specifically, we have shown that decision schemes based on continuous updating and variable decision times significantly improve speed while maintaining the desired high readout accuracy. This should be contrasted to previously considered fixed-time integration strategies. In the case of the *hunchback* promoter in the fly embryo, the continuous update schemes achieve the 2% EL positional resolution in less than 1 minute, always outperforming fixed-time integration strategies for the same promoter architecture (see SI Table 1). While 1 minute is even beyond what is required for the fly embryo, this margin in speed allows to accommodate additional constraints, viz. steep spatial boundary and biophysical constraints on kinetic parameters. Our approach ultimately yields many promoter architectures that are consistent with experimental observables in fly embryos, and results in decision times that are compatible with a precise readout even for the fast nuclear cycle 11 [8, 34].

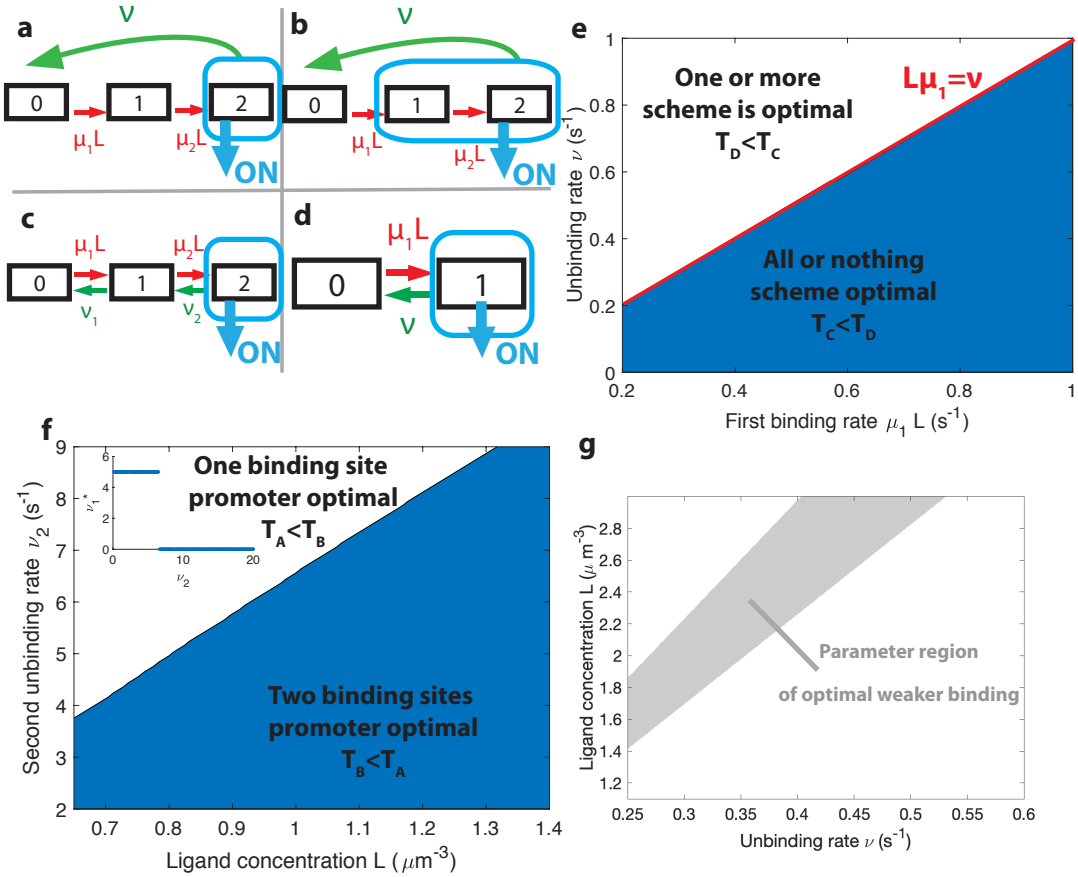

Figure 5: **The effects of different promoter architectures on the mean decision time.** We compare promoters of different complexity: the all-or-nothing $k = 2$ out-of-equilibrium model (**a**), the 1-or-more $k = 1$ out-of-equilibrium model (**b**), the two binding site all-or-nothing $k = 2$ equilibrium model (**c**) and the one binding site equilibrium model (**d**). **e**. Comparison of the mean decision time between $k = 2$ (**a**) and $k = 1$ (**b**) activation schemes for the two binding site out-of-equilibrium models as a function of the unbinding rate ν and binding rate μ_1. The binding rate μ_2 is fixed to $\mu_2 = \mu_1/2$. The fastest decision-making solution associates the second binding with slower variables to maximize V. Along the line $L\mu_1 = \nu$ the activation rules $k = 1$ and $k = 2$ perform at the same speed. $e = 10\%$. **f**. Comparison of the mean decision time for equilibrium architectures with one (**d**) and two (**c**) equilibrium TF binding sites. μ_1, μ_2, ν_1 are optimized at fixed ν_2, $e = 5\%$. We set a maximum value of 5 $\mu m^3 s^{-1}$ for μ_1 and μ_2, corresponding to the diffusion limited arrival at the binding site. For ν_1, the maximum value of 5s^{-1} corresponds to the inverse minimum time required to read the presence of a ligand, or to differentiate it from unspecific binding of other proteins. Additional binding sites are beneficial at high ligand concentrations and for small unbinding rates. In the blue region, the fastest mean decision time for a fixed accuracy assuming equilibrium binding, comes from a two binding site architecture with a non-zero first unbinding rate. In the white region, one of the binding rates $\to 0$ (see inset), which reduces to a one binding site model. $e = 5\%$. **g**. Weaker binding sites can lead to faster decision times within a range of parameters (gray stripe). We consider the $k = 1$ activation scheme with two binding sites (**b**.). For fixed L (x axis), ν (y axis) and $\mu_1 = 0.2\ \mu m^3 s^{-1}$, we optimize over μ_2 while setting $\mu_2 < \mu_1$ (context of diffusion limited first and second bindings). The gray regions corresponds to parameters for which the optimal second unbinding rate $\mu_2^* < \mu_1$ and the second binding is weak. In the white region $\mu_2^* = \mu_1$. For all panels $L_2 = L$, $L_1 = 0.95L$, $e = 0.05$.

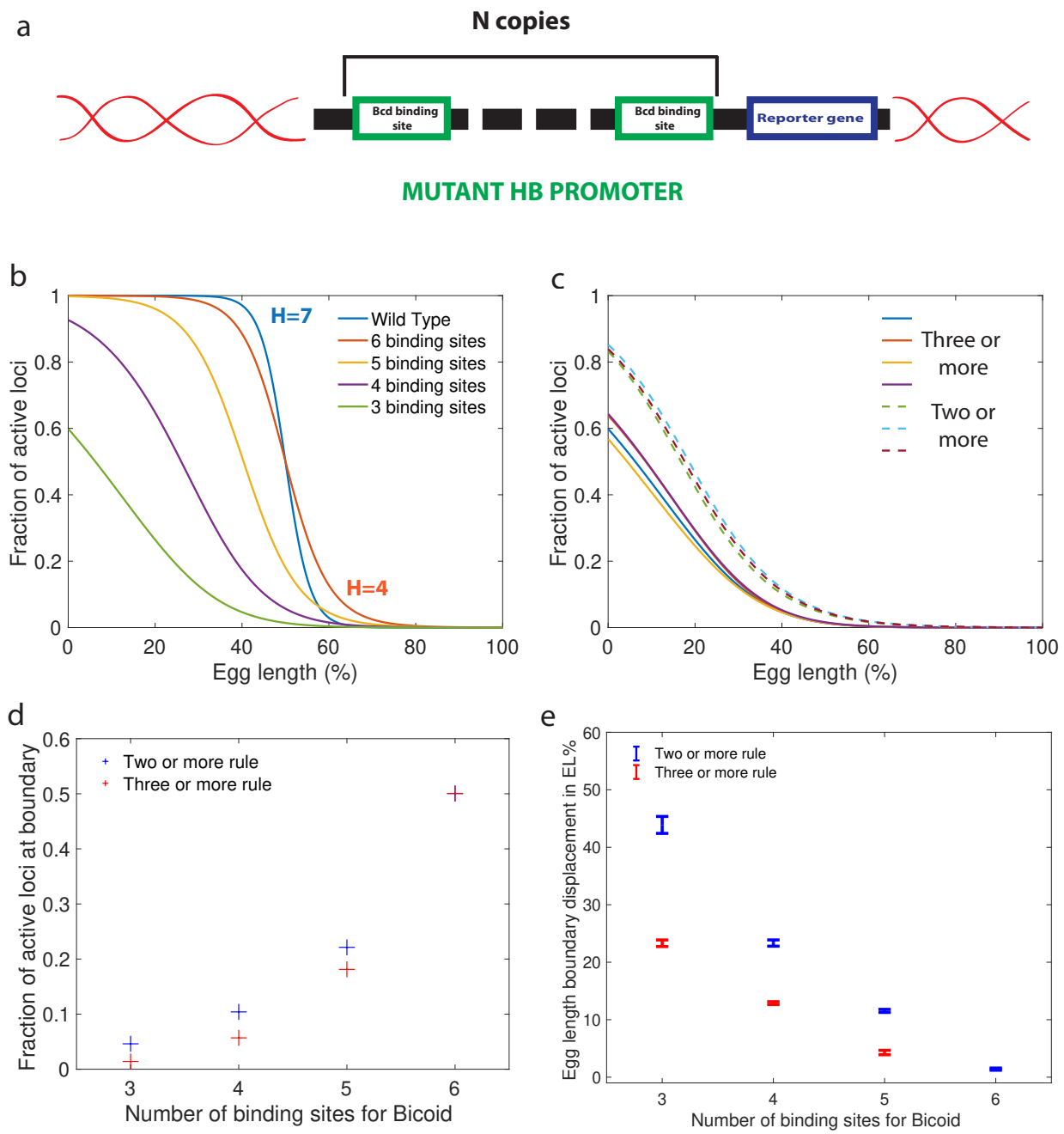

Figure 6: **Predictions for experiments with synthetic *hb* promoters. a.** We consider experiments involving mutant *Drosophilae* where a copy of a subgroup of the Bicoid binding sites of the *hunchback* promoter is inserted into the genome along with a reporter gene to measure its activity. **b.** The prediction for the activation profile across the embryo for wild type and mutants for the fastest decision time architecture for $H > 4$ and $k = 3$. **c.** The gene activation profile for several architectures for $H > 4$ and $k = 3$ (full lines) and $k = 2$ (dashed lines) that results in mean decision times < three minutes. Groups of profiles gather in two distinct clusters. **d.** Fraction of genes that are active on average at the hb expression boundary using the minimal $\langle T \rangle$ architecture identified for $H > 4$ and $k = 3$ as a function of the number of binding sites in the *hb* promoter. **e.** Predicted displacement of the boundary region defined as the site of half *hunchback* expression in terms of egg length as a function of the number of binding sites. The architectures shown result in the fastest decisions for $H > 4$ and $k = 2$ and $k = 3$. Error bar width is the standard deviation of the various architectures that are close to minimal $\langle T \rangle$. For all panels, $L(x)$ has an exponentially decreasing profile with decay length one fifth of total egg length with $L_0 = 5.6\ \mu m^{-3}$ at the boundary. Parameters are given in Appendix H.

Several arguments have been brought forward to suggest that the duration of a nuclear cycle is the limiting time period for the readout of Bicoid concentration gradient. The first one concerns the reset of gene activation and transcription factor binding during mitosis. In that sense, any information that was stored in the form of Bicoid already bound to the gene is lost. The second argument is that the hunchback response integrated over a single nuclear cycle is already extremely precise. However, none of these imply that the *hunchback* decision is made at a fixed time (corresponding to mitosis) so that strategies involving variable decision times are quite legitimate and consistent with all the known phenomenology.

We have performed our calculations in a worst-case scenario. First, we did not consider averaging of the readout between neighbouring nuclei. While both protein [23] and mRNA concentrations [57] are definitely averaged, and it has been shown theoretically that averaging can both increase and decrease [24] readout variability between nuclei, we do not take advantage of this option. The fact that we achieve less than three minutes in nuclear cycle 11, demonstrates that averaging is *a priori* dispensable. Second, we demand that the *hunchback* promoter results in a readout that gives the positional resolution observed in nuclear cycle 14, in the time that the *hunchback* expression profile is established in nuclear cycle 11. The reason for this choice is twofold. On the one hand, we meant to show that such a task is possible, making feasible also less constrained set-ups. On the other hand, the *hunchback* expression border established in nuclear cycle 11 does not move significantly in later nuclear cycles in the WT embryo, suggesting that the positional resolution in nuclear cycle 11 is already sufficient to reach the precision of later nuclear cycles. The positional resolution that can be observed in nuclear cycle 11 at the gene expression level is $\sim 10\%$ EL [34], but this is also due to smaller nuclear density.

Two main factors generally affect the efficiency of decisions: how information is transmitted and how available information is decoded and exploited. Decoding depends on the representation of available information. Our calculations have considered the issue of how to convey information across the bottleneck of gene activation, under the constraint of a given Hill coefficient. The latter is our empirical way of taking into account the constraints imposed by the decoding process. High Hill coefficients are a very convenient way to package and represent positional information: decoding reduces to the detection of a sharp transition, an edge in the limit of very high coefficients. The interpretation of the Hill coefficient as a decoding constraint is consistent with our results that an increase in the coefficient slows down the decision time. The resulting picture is that promoter architecture results from a balance between the constraints imposed by a quick and accurate readout and those stemming from the ease of its decoding. The very possibility of a balance is allowed by the main conclusion demonstrated here that promoter structures can go significantly below the time limit imposed by the duration of the early nuclear cycles. That leaves room for accommodating other features without jeopardising the readout timescale. While the constraint of a fixed Hill coefficient is an effective way to take into account constraints on decoding, it will be of interest to explore in future work if and how one can go beyond this empirical approach. That will require developing a joint description for transmission and decoding via an explicit modeling of the mechanisms downstream of the activation bottleneck.

Recent work has shed light on the role of out of equilibrium architectures on steepness of response [45] and gradient establishment [34, 53]. Here, we showed that equilibrium architectures perform very well and achieve short decision times, and that out of equilibrium architectures do not seem to significantly improve the performance of promoters, except for making some switches from gene states a bit faster. Non-equilibrium effect can, however, increase the Hill coefficient of the response without adding extra binding sites, which is useful for the downstream readout of positional information that we formulated above as decoding.

We also showed how short bound times of Bicoid molecules to the DNA [52] are translated into accurate and fast decisions. Our fast decision-making architectures also display short DNA-bound times. However, the constraint of high cooperativity means that the distribution of bound times to the DNA is non-exponential and the rare long binding times that occur during the bursty binding process are exploited during the read-out. The combination of high cooperativity and high temporal variance due to bursty dynamics is a possible recipe for an accurate readout.

At the technical level, we developed new methods for the mean decision time of complex gene architectures within the framework of variable time decision-making (SPRT). This allowed us to establish the equality $V = D$ between drift and diffusion of the log-likelihood between two close hypotheses. Its underlying reason is the martingale property that the conditional expectation of probabilities for two hypotheses, given all prior history, is equal to their present value. The methodology developed here will be useful for the broad range of decision processes where SPRT is relevant. The general rules for building efficient readout mechanisms that we discussed here could be relevant for synthetic biology.

Finally, we made predictions about how promoter architectures with different activation schemes can be compared in synthetic embryos with different numbers of Bcd binding sites. Furthermore, experiments that change the composition of the syncytial medium would influence the diffusion constant and assay the assumption of diffusion-limited activation. Our model predicts that these changes would result in modifications of *hunchback* activation profiles: higher or lower diffusion rates slide the *hunchback* profile towards the anterior or the posterior end of the embryo, respectively, similarly

to an increase or a decrease of the number of Bicoid binding sites. Any of the above experiments would greatly advance our understanding of the molecular control of spatial patterning in *Drosophila* embryo and, more generally, of regulatory processes.

Acknowledgements: We are grateful to Gautam Reddy and Huy Tran for multiple relevant discussions.

Appendices

A Biological parameters in the embryo

To build a model of the promoter, we combine parameters from recent experimental work.

The embryo at nuclear cycle n is modelled as having 2^{n-1} nuclei/cells. For simplicity we assume they are equidistributed on the periphery of the embryo and across the embryo's length and do not take into account the effect of the geometry of the embryo because the curvature of the embryo is small (the embryo is about $500\mu m$-long along the anterior-posterior axis and only about $100\mu m$-long along the Dorso-ventral axis). We also neglect the few nuclei forming pole cells and remaining in the bulk [51].

The Bicoid concentration in the embryo is given by $L(x) = L_0 e^{-(x-x_0)/\lambda}$, where x is the position along the anterior-posterior (AP) embryo axis measured in $\%$ of the egg length, λ is the decay length also measured in $\%$ of the egg length ($\lambda \simeq 100\mu m$ which is roughly 20% of the egg length [12]) and x_0 is the position of half-maximum *hunchback* expression (x_0 is of the order of $250\mu m$ and varies slightly depending on cell cycle, usually close to 45% egg length for the WT *hunchback* promoter [13]). $L_0 \simeq 5.6\mu m^{-3}$ is the concentration of free Bicoid molecules at the AP boundary [58] (that also corresponds to the point of largest *hunchback* expression slope [34]).

To compute the diffusion limited arrival rate at the locus, we use the following parameters: diffusivity $D \simeq 7.4\mu m^2 s^{-1}$ [13, 58], concentration of free Bicoid molecules at the AP boundary L_0, size of the binding target $a \simeq 3nm$ [23], which leads to an effective $\mu_{\max} L_0 = DaL_0 \simeq 0.124 s^{-1}$ at the boundary. This value is an upper bound, assuming that every encounter between a transcription factor and a binding site results in successful binding. We note in Fig. 4 b that most of the ON rates are close to the diffusion limit. We conclude that in this parameter regime, the most efficient strategy is to have ON events that are as fast as possible. The only reason to reduce them is to achieve the required Hill coefficient. That can be done by either adjusting the ON or the OFF rates.

The above estimate $\mu_{\max} L_0 = 0.124\text{s}^{-1}$ may be inaccurate for various reasons and we ought to explore the sensitivity of results to those uncertainties. Table 1 recapitulates the time-performance of different strategies for different choices of the parameters. A first source of uncertainty is the value of the diffusivity, which is estimated to vary between 4 and $7\mu m^2 s^{-1}$ [13, 58]. We consider then two possible values for the diffusivity from [13]: $D_1 = 4.5\mu m^2 s^{-1}$ and the aforementioned value $D_2 = 7.4\mu m^2 s^{-1}$. A second source of uncertainty is that the actual Bicoid concentration at the boundary could vary by up to a factor two depending on estimates of the concentration and its decay length [12, 58, 34]. We consider then two possible value for the concentration: the aforementioned $L_0^{(1)} = 5.6$ molecules per μm^3, and $L_0^{(2)} = 11.2$ molecules per μm^3. Finally, we assumed above that the size of the target is the full Bicoid operator site, which we took about ten base pairs following Ref. [23]. However, assuming that the TF must reach a specific position on the promoter binding site could reduce the size of the target to a single base pair, that is a by a factor 10. In terms of parameters, we consider then two possible values for a : either $a_1 \simeq 3.10^{-4}\mu m$, or $a_2 = 3.10^{-3}\mu m$. All in all, taking into account the various sources of uncertainty $\mu_{\max} L_0$ can range in the interval $[0.0076, 0.25] s^{-1}$.

We consider four possible decision strategies. The first one is a single binding site making a fixed-time decision. This computation is made using the original Berg-Purcell formula [17]. In the Berg-Purcell strategy, the concentration of the ligand is inferred based on the total time that the receptor or the binding site has spent occupied by ligands. Due to averaging, the relative error of the concentration readout is inversely proportional to the number of independent measurements of the concentration that can be made within the total fixed time T, i.e. to the arrival rate of new Bicoid molecules at the binding site, multiplied by the probability to find the binding site empty (in our case, at the boundary, the probability is roughly one half). Since the rate of arrival of new Bicoid molecules to the binding site is $\mu_{\max} L_0 = DaL_0$, the relative error of the concentration readout is given by

$$\frac{\delta L_0}{L_0} = \sqrt{\frac{1}{2(1-\bar{n})DaL_0 T}} \ , \tag{8}$$

where L_0 is the estimate of the concentration, T is the integration time and $\bar{n}$ is the probability that the binding site is full.

In the second strategy, there are 2 sets of 6 binding sites being read independently. In that case, the information from each binding site can be accessed individually and their contributions averaged to give a more precise estimate. This calculation again can be made using the original Berg-Purcell formula [17] for several receptors, dividing the relative

	a_1				a_2			
	D_1		D_2		D_1		D_2	
	$L_0^{(1)}$	$L_0^{(2)}$	$L_0^{(1)}$	$L_0^{(2)}$	$L_0^{(1)}$	$L_0^{(2)}$	$L_0^{(1)}$	$L_0^{(2)}$
Berg-Purcell one operator site	4.0 h	100 min	117 min	59 min	20 min	10 min	12 min	5.9 min
Berg-Purcell twelve operator sites independently read	58 min	29 min	34 min	17 min	5.8 min	2.9 min	3.4 min	1.7 min
Optimal equilibrium architecture fixed-time decision ($e = 0.32$)	24 min	13 min	15 min	7.7 min	2.8 min	1.6 min	1.8 min	1.1 min
Optimal equilibrium architecture SPRT decision ($e = 0.32$)	17 min	8.5 min	9.9 min	5.0 min	1.7 min	51s	1.0 min	30s

Table 1: Mean decision times for various choices of parameters and four different decision processes (see sections A and B). For the optimal architectures identified (third and fourth lines of the table) we take the fastest architectures without any constraints on the slope. These architectures systematically use the activation rule $k = 1$. Highlighted in red are the results for the range of parameters presented in the text. All calculations are made with $e = 32\%$, $L = L_1 = 1.05 \cdot L_0$, $L_2 = 0.95 \cdot L_0$. The diffusion limited ON rate is $\mu_{\max} L_0 = DaL_0$. For the two Berg-Purcell architectures, both the ON rate and OFF rate per site are equal to $\mu_{\max}$. For the optimal architectures we have $\mu_i L_0 = \mu_{\max} L_0 \cdot (7 - i)$ and $\nu_i = i \cdot \mu_{\max} L_0 \cdot 0.5^{1/6}/(1 - 0.5^{1/6})$ to keep half the genes active at the boundary.

error by the square root of the total number of binding sites in Eq. 8:

$$\frac{\delta L_0}{L_0} = \sqrt{\frac{1}{2N(1-\bar{n})DaL_0T}}, \tag{9}$$

where N is the total number of binding sites (in our case, $N = 12$).

For the third possibility, we consider a decision made at a fixed time using the fastest architecture identified (Fig. 4) without constraint on the slope (activation rule $k = 1$). We compute the decision time using the drift-diffusion approximation with fixed time (see Appendix B).

Finally, we consider the fastest architecture identified with a random decision time and the Sequential Probability Ratio Test (SPRT) strategy.

The result of the above calculations is that for a single receptor estimating Bcd concentration with 10% precision within a fixed-time Berg-Purcell type calculation (see section B), decisions take between 6 min for the fastest binding rates and ~ 4 hours for the slowest estimates. Conversely, by using the on-the-fly SPRT decision-making process and the 1-or-more $k = 1$ scheme at equilibrium, the time needed to make decisions with 10% precision and an error rate of 32% at the boundary is $\simeq 30$s for the fastest rates and $\simeq 17$ minutes for the slowest rates. For all sets of parameters, the on-the-fly SPRT decision-making process gives a ~ 3.5-fold faster decision time than the $N = 12$ Berg-Purcell estimate and a > 10-fold faster decision making time than the one-binding-site Berg-Purcell estimate. For the fastest rates, a decision with an error rate of less than 5% can be achieved in about 5 minutes within the SPRT scheme.

B Error rate and decision time for the fixed-time decision strategy

In this section we describe how we compute the decision time for a fixed-time strategy (or "Berg-Purcell type decision") and a complex promoter architecture.

The classic Berg-Purcell calculation is based on the idea of averaging the time spent by the ligand bound to a receptor (or, in our case, a binding site). The original calculation assumed that the waiting times between binding and unbinding

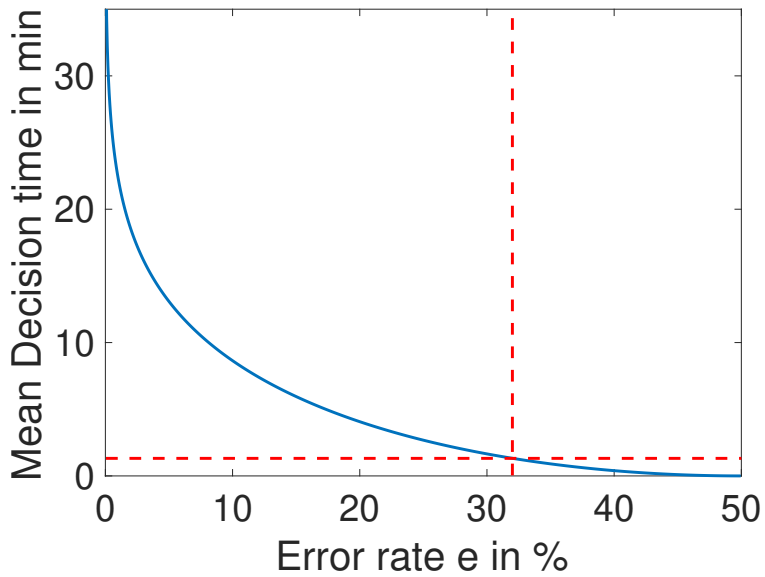

Figure 7: **The mean decision time as a function of the error rate e for the fastest architecture identified with $H > 5$ and $k = 1$ (see Fig. 4a)**. When the error rate is 32%, decisions are made in less than a minute (red dashed lined). Parameters are $L = L_1 = 1.05 \cdot 5.6\mu m^{-3}$, $L_2 = 0.95 \cdot 5.6\mu m^{-3}$, $\mu_1 = 0.13\mu m^3 s^{-1}$, $\mu_2 = 0.11\mu m^3 s^{-1}$, $\mu_3 = 0.086\mu m^3 s^{-1}$, $\mu_4 = 0.066\mu m^3 s^{-1}$, $\mu_5 = 0.043\mu m^3 s^{-1}$, $\mu_6 = 0.022\mu m^3 s^{-1}$, $\nu_1 = 4.5 s^{-1}$, $\nu_2 = 0.042 s^{-1}$, $\nu_3 = 0.11 s^{-1}$, $\nu_4 = 0.033 s^{-1}$, $\nu_1 = 0.037 s^{-1}$, $\nu_1 = 0.053 s^{-1}$.

are exponential and that the bound times are not informative about the concentration. Neither of these assumptions hold in the case of the *hunchback* promoter. Indeed, in the context of a complex promoter architecture, the waiting times that are available to the nucleus or cell downstream are the gene's ON and OFF switching times. They are not exponentially distributed, and, depending on the activation rule, the OFF times can be just as informative about the concentration as the ON times. For these two reasons, we ought to readapt the Berg-Purcell idea to compute the mean decision time.

To that purpose, we consider a decision with a given rate of error e, fix a time of decision T and choose the concentration that has the highest likelihood between the two options L_1 and L_2. In other words, if $\log R(T) = \log P(L_1)/P(L_2) > 0$ then the nucleus chooses $L = L_1$, while if $\log R(T) < 0$ then it chooses $L = L_2$. For instance, if the actual concentration $L = L_1$, then the probability of error at time T is given by $P(\log R(t) < 0)$.

To calculate the above error, we use the drift-diffusion approximation for $\log R(t)$, compute the drift V and diffusivity D from Eq. 1-4 and approximate the distribution of $\log R(T)$ by a normal distribution with mean VT and standard deviation $\sqrt{DT}$. We compute the error rate e for the fixed-time decision process based on the Gaussian approximation. Finally, to find the mean decision time for a given error rate, we perform a quick one-dimensional search over T, which yields the value of the fixed decision time appropriate for the prescribed error e.

C The mean first-passage time for the decision-making process

To investigate the role of promoter architectures in decision-making, we apply the SPRT approach (Sequential Probability Ratio Test) [26, 27]. In the simplest formulation of this approach, a decision is made between two hypotheses about the concentration of a surrounding TF: either the TF is at concentration L_1 or it is at concentration L_2. The decision is based on the binding and unbinding events of the TF to a promoter. At each point in time, the error of committing to a given concentration (scenario) is estimated by computing the ratio $R(t)$ of the probability of one hypothesis, $P(L_1)$ (the surrounding concentration is L_1) over the other (the concentration is L_2), $P(L_2)$:

$$R(t) = \frac{P(L_1)}{P(L_2)} \,. \tag{10}$$

Technically, the time dependent likelihood ratio, $R(t)$ undergoes a random walk as TFs bind and unbind to the promoter, activating and deactivating the gene. The process is terminated and a decision is made when the likelihood ratio falls below the desired error level, which is expressed in terms of absorbing boundaries at K_+ (the concentration is L_1) and K_- (the concentration is L_2): $\log R(t) \leq K_-$ or $\log R(t) \geq K_+$ (see Fig. 1.1). The boundaries $K_\pm$ can be expressed

in terms of the error e and for symmetric errors, $K_+ = -K_- = (1-e)/e$ [27]. In our case $e = 32\%$. The mean time for decision can be computed for each discrimination task as the mean first-passage time of a random walk (in the limit of long decision times). In Fig. 7 we show the mean decision-time for different values of e.

Assuming the gene has two levels of activation ON and OFF, the information available to downstream mechanisms is a series of ON times s_i and OFF times t_j of gene activity. The probability of a concentration hypothesis is then $P(L_m) = P(\{t_i\}, \{s_j\}|L_m)$. If successive ON and OFF times are independent then the probabilities factorize. The log ratio is then written as a function of the ON (respectively OFF) time probability distribution $P_{\rm ON}(t, L)$ (respectively $P_{\rm OFF}(t, L)$)

$$\log R(t) = \sum_{i=1}^{J_-} \left(\log P_{\rm ON}(s_i, L_1) - \log P_{\rm ON}(s_i, L_2)\right) + \sum_{i=1}^{J_+} \left(\log P_{\rm OFF}(t_i, L_1) - \log P_{\rm OFF}(t_i, L_2)\right), \quad (11)$$

where J_- is the number of ON to OFF switching events and J_+ the number of OFF to ON switching events [27]. To understand the dynamics of the log ratio, it is necessary to compute the distributions $P_{\rm ON}(t, L)$ and $P_{\rm OFF}(t, L)$ based on the promoter dynamics, which is the focus of the following subsection.

C.1 From binding to gene activation

In this section we describe how the high-dimensional complete state of the promoter is mapped onto the low-dimensional activity of the gene. We use a formalism similar to that of Refs. [11, 34].

The promoter features N binding sites : its complete state at time t is described by an N dimensional vector $\vec{B}(t)$, where $B_i = 0/1$ if the binding site i is empty/full. We assume the gene has two levels of activity: either it is OFF and no mRNA is produced, or it is ON and mRNA is produced at a fixed rate. Activity is then described by a simple Boolean variable $a(t)$ equal to $0/1$, corresponding to the gene being OFF/ON.

We also assume that the activity of the gene depends only on the total number of transcription factors bound to the promoter so that there is an integer $1 \leq k \leq N$ such that $a(t) = \mathbb{1}_{\sum_i B_i \geq k}$ (where $\mathbb{1}$ is the indicator function). From the point of view of gene activity, we are only interested in the dynamics of $\mathbf{B}(t) = \sum_i B_i(t)$. We make another simplifying assumption: the probabilities of $\mathbf{B}(t)$ increasing or decreasing only depend on the value of $\mathbf{B}(t)$ and not on which binding sites specifically are bound or unbound, that is $\mathbf{B}(t)$ itself has a Markovian dynamics in $\{0, 1, ...N\}$.

At a given time t, we describe the stochastic state of the promoter as a vector of probability $\vec{X}(t)$ where $X_i(t)$ is the probability of having $\mathbf{B} = i-1$ and $\sum_i X_i(t) = 1$. The Markovian dynamics of $\mathbf{B}$ translate into an $(N+1) \times (N+1)$ transition matrix M for $\vec{X}$: $\vec{X}(t+s) = e^{Ms}\vec{X}(t)$. M describes the dynamics of the promoter from the point of view of gene activity. If transcription factors do not dimerize or form complexes, then $M_{i,j} \neq 0$ only if $|i-j| \leq 1$ since the probability of two of them binding or unbinding decreases as the square of time for short times.

Let us now relate the statistics of the switching times for the gene activity a to the transition matrix M. Starting from a distribution of OFF states $\vec{X}_0$ we compute the cumulative distribution function of the waiting time τ before switching to the ON state

$$P(\tau \leq t) = \mathrm{Trans}(\vec{X}_{\rm ON}) e^{M^*_{\rm OFF} t} \vec{X}_0, \quad (12)$$

where Trans is the transpose, $\vec{X}_{\rm ON}$ is a vector of 1 for states corresponding to active genes and 0 for states corresponding to inactive genes, and $M^*_{\rm OFF}$ is a modified version of M where all ON states act as "sinks" (i.e. all the transition rates from ON states have been set to 0). The expression in Eq. 12 computes the cumulative probability of transitions to an ON state before time t, that is $P_{\rm OFF}(t) = dP(\tau \leq t)/dt$.

For simplicity, we restrict ourselves to promoter structures where there is only one point of entry into the ON or the OFF states (i.e. any switching event from ON to OFF or *vice versa* will end with the promoter having a specific number of binding sites). Under this hypothesis, the probability vector $\vec{X}_0$ in Eq. 12 is uniquely determined and independent of the specific dynamics of the previous ON or OFF times. We relax these constraints on the promoter structure in Appendix G. We denote by $\tau_{\rm OFF}$ (respectively $\tau_{\rm ON}$) the average of the OFF (respectively ON) times for the real concentration L.

C.2 Random walk of the log ratio

When the two hypothesized concentrations are very similar to each other as compared to the concentration scale L set by the actual concentration value, $|L_1 - L_2| << L$, the discrimination is hard and requires a large number of binding and unbinding events. In this limit, the random walk $\log R(t)$ can be approximated by a drift-diffusion process with drift V and diffusion D:

$$\partial_t \log R(t) = V + \sqrt{2D}\eta, \quad (13)$$

where η is a Gaussian white noise. The decision time for the case of symmetric boundaries $K_+ = -K_-$ is a random variable T with mean given by Eq. 1 in the main text [27]. $\langle T \rangle$ depends on the details of the biochemical sensing of the TF concentration and promoter architecture via the drift and diffusivity. Computing V and D in Eq. 13 is enough to derive the mean first-passage time to the decision and even its full distribution by computing its Laplace transform as a solution of the drift-diffusion equation using standard techniques of first-passage for Gaussian processes [27].

C.3 Drift

For many switching events $J^+ >> 1$ and $J^- >> 1$, the sums in Eq. 11 can be replaced by continuous averages over binding time distributions. Since J_- and J_+ differ at most by one, we can also replace the two values $J_- \simeq J_+$ by a unique value J, which is the number of ON-OFF cycles. The times are distributed according to the ON and OFF probability distributions for the real concentration L. At a given large time t, the number J of terms in the sum and the log-ratios appearing in Eq. 11 are a priori correlated but Wald's equality [26] ensures that the average of the sum is the product of the two averages. Since the expected number of cycles grows linearly in time as $\langle J \rangle \propto t/\left(\tau_{\rm ON} + \tau_{\rm OFF}\right)$, we conclude that the drift term in Eq. 13 is given by :

$$
\begin{aligned}
V &= \frac{\langle J \rangle}{t} \times \langle \log P_{\rm ON}(t, L_1) - \log P_{\rm ON}(t, L_2) + \log P_{\rm OFF}(t, L_1) - \log P_{\rm OFF}(t, L_2) \rangle_L \\
&= \frac{1}{\tau_{\rm ON} + \tau_{\rm OFF}} \left[\int_0^{+\infty} dt P_{\rm ON}(t, L) \left(\log \frac{P_{\rm ON}(t, L_1)}{P_{\rm ON}(t, L)} - \log \frac{P_{\rm ON}(t, L_2)}{P_{\rm ON}(t, L)} \right) \right. \\
&\left. + \int_0^{+\infty} dt P_{\rm OFF}(t, L) \left(\log \frac{P_{\rm OFF}(t, L_1)}{P_{\rm OFF}(t, L)} - \log \frac{P_{\rm OFF}(t, L_2)}{P_{\rm OFF}(t, L)} \right) \right] \\
&= \frac{1}{\tau_{\rm OFF} + \tau_{\rm ON}} \left[D_{KL}(P_{\rm OFF}(., L) || P_{\rm OFF}(., L_2)) - D_{KL}(P_{\rm OFF}(., L) || P_{\rm OFF}(., L_1)) \right. \\
&\left. + D_{KL}(P_{\rm ON}(., L) || P_{\rm ON}(., L_2)) - D_{KL}(P_{\rm ON}(., L) || P_{\rm ON}(., L_1)) \right],
\end{aligned}
\tag{14}
$$

where $D_{KL}(P||Q) = \int_0^\infty ds P(s) \log\left(P(s)/Q(s)\right)$ is the Kullback-Leibler divergence between the two distributions P and Q.

In sum, the drift is determined by how informative the distribution of waiting times in the ON and OFF states are about the concentration differences, with an average rate equal to the inverse of the cycle time $\tau_{\rm OFF} + \tau_{\rm ON}$. The Kullback-Leibler divergence appearing in Eq. 14 is intuitive : it represents the distance between the real concentration and the hypothetical concentration in the space of probabilistic models of switching times. The larger that distance, the easier it becomes to tell the difference between the two distributions through random sampling.

C.4 Expansion of the drift for small concentration differences

When the two candidate concentrations are similar, $L \simeq L_1 \simeq L_2$, the quantities computed in the previous subsection can be expanded at first order in the differences in concentrations $\delta L_1 = L_1 - L$ and $\delta L_2 = L_2 - L$. Starting from Eq. 14, we expand the drift V at first and second orders:

$$
\begin{aligned}
V(\tau_{\rm ON} + \tau_{\rm OFF}) &= \int_0^{+\infty} dt P_{\rm OFF}(t, L) \left[\log \frac{P_{\rm OFF}(t, L_1)}{P_{\rm OFF}(t, L)} - \log \frac{P_{\rm OFF}(t, L_2)}{P_{\rm OFF}(t, L)} \right] + \hookrightarrow_{P_{\rm ON}} \\
&= \int_0^{+\infty} dt P_{\rm OFF}(t, L) \left[\log \frac{P_{\rm OFF}(t, L) + \delta L_1 \partial_L P_{\rm OFF}(t, L) + \delta L_1^2 \partial_{L,L}^2 P_{\rm OFF}(t, L)/2}{P_{\rm OFF}(t, L)} \right] \\
&- \int_0^{+\infty} dt P_{\rm OFF}(t, L) \left[\log \frac{P_{\rm OFF}(t, L) + \delta L_2 \partial_L P_{\rm OFF}(t, L) + \delta L_2^2 \partial_{L,L}^2 P_{\rm OFF}(t, L)/2}{P_{\rm OFF}(t, L)} \right] + \hookrightarrow_{P_{\rm ON}} \\
&= \delta L_1 \int_0^{+\infty} dt \partial_L P_{\rm OFF}(t, L) + \frac{\delta L_1^2}{2} \int_0^{+\infty} dt \partial_{L,L}^2 P_{\rm OFF}(t, L) - \int_0^{+\infty} dt \frac{\delta L_1^2}{2} \frac{\left(\partial_L P_{\rm OFF}(t, L)\right)^2}{P_{\rm OFF}(t, L)} \\
&- \delta L_2 \int_0^{+\infty} dt \partial_L P_{\rm OFF}(t, L) - \frac{\delta L_2^2}{2} \int_0^{+\infty} dt \partial_{L,L}^2 P_{\rm OFF}(t, L) + \int_0^{+\infty} dt \frac{\delta L_2^2}{2} \frac{\left(\partial_L P_{\rm OFF}(t, L)\right)^2}{P_{\rm OFF}(t, L)} \hookrightarrow_{P_{\rm ON}},
\end{aligned}
\tag{15}
$$

where $\hookrightarrow_{P_{\rm ON}}$ means that the same operations and integrations are performed for $P_{\rm ON}$.

Due to conservation of probability, the integral of the first and second L-derivatives of $P_{\rm OFF}(t,L)$ vanish. The first-order expansion of V vanishes and we have at first non-vanishing order in $|L_i - L|$

$$V = \frac{1}{2(\tau_{\rm ON}+\tau_{\rm OFF})}\left[\int_0^{+\infty} dt \frac{(\partial_L P_{\rm OFF}(t,L))^2}{P_{\rm OFF}(t,L)}\right]\left[\delta L_2^2 - \delta L_1^2\right] + \hookrightarrow_{P_{\rm ON}} . \tag{16}$$

If for instance $|L_2 - L| > |L_1 - L|$ then the drift is positive, favouring the concentration L_1, closer to the real concentration.

C.5 Equality between drift and diffusivity

In this section we present different ways of proving the equality between V and D in SPRT when the two hypotheses are close by connecting different approaches. We show that this equality is a general property of random walks in Bayesian belief space. We check that these results are true in the controlled case of one binding site in Fig. 8.

First approach: the exit points of the decision process. As proved by Wald in the original paper where he introduced sequential probability ratio tests [59], the nature of the test (the ratio between the likelihood of two hypotheses) requires a specific relationship between the error and the boundaries that define the regions of decision. In our case, we assume the same probability of calling L_1 when L_2 is true and calling L_2 when L_1 is true, leading to the definition of only one error level e and two symmetric boundaries K and $-K$. Specifically Wald shows that $K = \log\frac{1-e}{e}$ (see also [27]).

When the two hypotheses are close enough that the variations of the log-likelihood can be approximated by a Gaussian process, one can compute the exit probabilities in terms of the drift V and diffusivity D. The equation for the probability of absorption $\Pi(X)$ at the upper boundary K is

$$\left[V\frac{d}{dx} + D\frac{d^2}{dx^2}\right]\Pi(x) = 0\,, \tag{17}$$

with the boundary condition $\Pi(K) = 1$ and $\Pi(-K) = 0$. The corresponding solution is

$$\Pi(x) = \frac{e^{\frac{VK}{D}} - e^{-\frac{-Vx}{D}}}{e^{\frac{VK}{D}} - e^{-\frac{-VK}{D}}}\,, \tag{18}$$

as shown in the supplementary material of [27]. Setting $x = 0$ in Eq. 18, we find that

$$\Pi(0) = \frac{e^{VK/D} - 1}{e^{VK/D} - e^{-VK/D}} = \frac{e^{VK/D}}{1 + e^{VK/D}}. \tag{19}$$

We note that this probability of absorption is also $1 - e$ by definition of the error (assuming for instance that $L = L_1$) leading to

$$e = \frac{1}{1 + e^{VK/D}}, \tag{20}$$

which in turn gives

$$e^{VK/D} = \frac{1-e}{e} = e^K. \tag{21}$$

And so we find that in the limit of close hypotheses, $V = D$.

Second approach: expansion for small concentration differences. Let us consider the SPRT process between two hypotheses L_1 and L_2 and assume for simplicity that $L = L_2$. In this version of the proof, we consider that the difference $\delta L = L_1 - L$ is small compared to L (i.e $\delta L/L << 1$) and expand the expressions for drift and diffusion in increasing orders of $\delta L/L$ to find that they match. We have shown in Appendix C.4 that the first non-vanishing term in the expansion of the drift is of order 2 in $\delta L/L$ and is given by Eq. 16. An integral formula for the second moment of the log-likelihood is given in Eq. A15 of [49] from which we get that the diffusivity of the log ratio is the sum of four terms. The first term is given by

$$D_1 = \frac{V^2}{(\tau_{\rm ON}+\tau_{\rm OFF})^3}\int_0^{+\infty} dt P_{\rm ON}(t,L)\int_0^{\infty} ds P_{\rm OFF}(s,L)(t+s)^2. \tag{22}$$

D_1 is proportional to V^2 and so is of order $(\delta L/L)^4$. The second term is given by

$$D_2 = \frac{-2V}{(\tau_{\rm ON}+\tau_{\rm OFF})^2}\left(\tau_{\rm ON}\int_0^{\infty} ds P_{\rm OFF}(s,L)\log\frac{P_{\rm OFF}(s,L_1)}{P_{\rm OFF}(s,L_2)} + \tau_{\rm OFF}\int_0^{\infty} dt P_{\rm ON}(t,L)\log\frac{P_{\rm ON}(t,L_1)}{P_{\rm ON}(t,L_2)}\right. \tag{23}$$
$$\left. + \int_0^{\infty} ds P_{\rm OFF}(s,L) s \log\frac{P_{\rm OFF}(s,L_1)}{P_{\rm OFF}(s,L_2)} + \int_0^{\infty} dt P_{\rm ON}(t,L) t \log\frac{P_{\rm ON}(t,L_1)}{P_{\rm ON}(t,L_2)}\right).$$

The prefactor V is of order $(\delta L/L)^2$. Expanding the first two terms in the brackets gives the same type of terms as in Eq. 15. Because of probability conservation we find that these terms are of the same order as V (i.e $(\delta L/L)^2$). The last two terms have prefactors s and t respectively which break the argument for vanishing first order terms in Eq. 15 and these terms are of order $\delta L/L$. Putting the pieces together, we find that D_2 is of order $(\delta L/L)^3$. The third term is given by

$$D_3 = (\tau_{\rm ON} + \tau_{\rm OFF})^{-1} \int_0^{+\infty} dt P_{\rm ON}(t, L) \int_0^{+\infty} ds P_{\rm OFF}(s, L) \left(\log \frac{P_{\rm ON}(t, L_1)}{P_{\rm ON}(t, L_2)} + \log \frac{P_{\rm OFF}(s, L_1)}{P_{\rm OFF}(s, L_2)} \right)^2 . \quad (24)$$

Because ON and OFF times are independent, cross terms in D_3 are products of two $\langle \log P(., L_1)/P(., L_2) \rangle$ and are of subleading order $(\delta L/L)^4$. Using the symmetry between $P_{\rm ON}$ and $P_{\rm OFF}$ we expand one of the square terms in D_3

$$\int_0^{+\infty} dt P_{\rm ON}(t, L) \left(\log \frac{P_{\rm ON}(t, L + \delta L)}{P_{\rm ON}(t, L)} \right)^2 = \int_0^{+\infty} dt P_{\rm ON}(t, L) \left(\delta L \frac{\partial_L P_{\rm ON}(t, L)}{P_{\rm ON}(t, L)} + O\left(\frac{\delta L}{L^2}^2 \right) \right)^2 \quad (25)$$
$$= \int_0^{+\infty} dt \frac{(\partial_L P_{\rm ON}(t, L))^2}{P_{\rm ON}(t, L)} + O(\frac{\delta L^3}{L^3}).$$

The fourth term is $-V^2$ which is of order $(\delta L/L)^4$. So we find that, at leading order, $D \simeq D_3$ which has the same expansion as V (see Eq. 16). And so we recover that for small concentration differences, $V = D$.

In the case of one binding site with ON rate μL and OFF rate ν we check that the formula from [49] gives the exact expression computed in [27]

$$D = \frac{\nu \mu L}{(\nu + \mu L)^3} \left(\mu^2 (L_2 - L_1)^2 + \frac{1}{2} \left(\log \frac{L_1}{L_2} \right)^2 (\nu^2 + \mu^2 L^2) + \mu (L_2 - L_1)(\nu - \mu L) \log \frac{L_1}{L_2} \right). \quad (26)$$

Replacing L_2 with L in Eq. 26 and expanding in $\delta L/L$ we have

$$D = \frac{\nu \mu L}{(\nu + \mu L)^3} \left(\mu^2 \delta L^2 + \frac{1}{2} \left(\frac{\delta L}{L} \right)^2 (\nu^2 + \mu^2 L^2) + \mu \delta L (\nu - \mu L) \frac{\delta L}{L} + o\left(\frac{\delta L^2}{L^2} \right) \right) \quad (27)$$
$$= \frac{\nu \mu L}{2(\nu + \mu L)^3} \frac{\delta L^2}{L^2} \left((\nu^2 + \mu^2 L^2) + \mu L \nu + o\left(\frac{\delta L^2}{L^2} \right) \right) = \frac{1}{\nu^{-1} + (\mu L)^{-1}} \frac{\delta L^2}{2L^2} + o\left(\frac{\delta L^2}{L^2} \right).$$

We identify the drift computed for the one binding site example in 1.2.2 of the main text and find that at first order drift and diffusivity are equal.

Third approach: general properties of Bayesian random walks. To understand the origin of the equality between drift and diffusion, we go back to the definition of SPRT as the update of the Bayesian beliefs in two competing hypotheses. We no longer condition the process on one hypothesis being true but rather on the probability that each one is true given the value of the log ratio a certain time point. A very general property of posterior distributions updated with evidence is that their average does not change. This martingale property of belief update can be shown in the following way: assume that the nucleus receives extra evidence θ with probability $p(\theta)$. Before that evidence comes, the probability that hypothesis 1 is true p_1 has a certain distribution $P(p_1)$. Then we have that the probability that hypothesis 1 is true varies as :

$$\langle p_1 | \theta \rangle = \int d\theta \int dp_1 P(p_1|\theta) p_1 p(\theta) = \int d\theta \int dp_1 p_1 P(p_1) p(\theta|p_1), \quad (28)$$

where we used Bayes rule. The integral of $p(\theta|p_1)$ over θ sums up to 1 and we are left with

$$\langle p_1 | \theta \rangle = \int dp_1 p_1 P(p_1) = \langle p_1 \rangle. \quad (29)$$

In the context of two hypothetical concentrations, we consider the normalized likelihood of the two hypotheses at time t: $Q_2(t) = P_2(t)/(P_1(t) + P_2(t))$ and $Q_1(t) = P_1(t)/(P_1(t) + P_2(t))$, where $P_i(t)$ is the likelihood that hypothesis i is true based on the evidence accumulated up to time t. The martingale property translates as

$$0 = \langle \Delta Q_2 \rangle = Q_1 \langle \Delta Q_2 \rangle_1 + Q_2 \langle \Delta Q_2 \rangle_2, \quad (30)$$

where $\langle \rangle_\alpha$ are averages taken assuming hypothesis α is true and ΔQ is the variation of Q through time (or accumulated evidence). We note that $Q_1 = e^{\mathcal{L}(t)}/(1 + e^{\mathcal{L}(t)})$ and $Q_2 = 1/(1 + e^{\mathcal{L}(t))}$, where $\mathcal{L}(t) = \log P_1(t)/P_2(t)$ is the log-likelihood ratio at a given time. We express the variations of the probabilities in terms of the log-likelihood so that

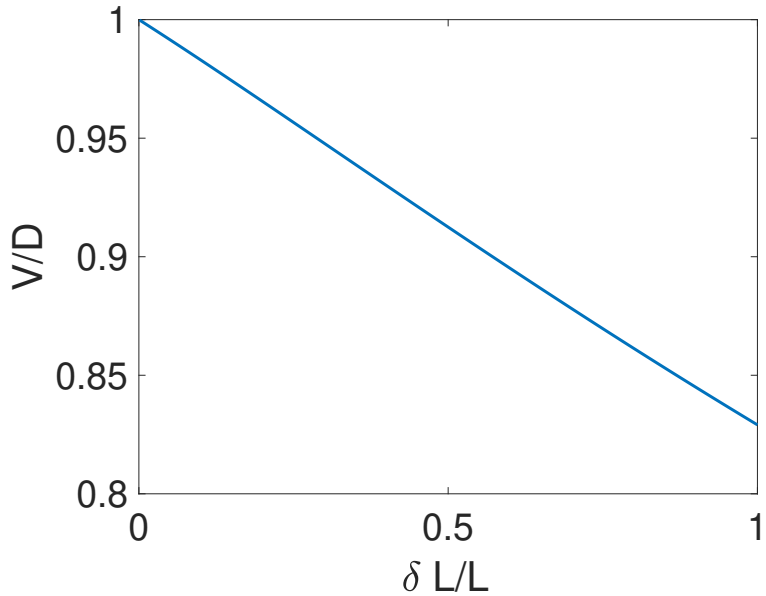

Figure 8: **The equality $V = D$ holds for close hypotheses** We compare the exact drift and diffusion computed from the formulae derived in [27] for the case of one binding site. We find that drift and diffusion are approximately equal for close concentrations (i.e small $\delta L/L$). Parameters are $\nu = 1\ s^{-1}$, $\mu = 1\ \mu m^3 s^{-1}$, $L_2 = L = 1\mu m^{-3}$, $L_1 = L + \delta L$.

we can connect it to the drift-diffusion parameters. The drift and diffusivity that depend a priori on the real concentration are respectively the average and variance of the variation of $\mathcal{L}$. We have $\langle \Delta\mathcal{L}(t)\rangle_1 = V_{(1)}\Delta t$, $\langle \Delta\mathcal{L}(t)\rangle_2 = V_{(2)}\Delta t$, $\langle (\Delta\mathcal{L}(t) - \langle\Delta\mathcal{L}\rangle_1)^2\rangle_1 = 2D_{(1)}\Delta t$ and $\langle (\Delta\mathcal{L}(t) - \langle\Delta\mathcal{L}\rangle_2)^2\rangle_2 = 2D_{(2)}\Delta t$ (where Δ is the total change over time Δt). When the two concentrations are close, the statistics of the acquisition of evidence are symmetric for L_1 and L_2 and we get that $D_{(1)} = D_{(2)} = D$ and $V_{(1)} = -V_{(2)} = V$. As explained in subsection 1.2.2 of the main text, computing the derivatives of Q_i with respect to $\mathcal{L}$ is straightforward. Plugging these relationships into Eq. 30 and gathering terms in V and D we find that

$$\begin{aligned} 0 &= \partial_{\mathcal{L}}\langle\Delta Q_2\rangle\left[Q_1\langle\Delta\mathcal{L}(t)\rangle_1 + Q_2\langle\Delta\mathcal{L}(t)\rangle_2\right] + \frac{1}{2}\partial^2_{\mathcal{L}}\langle\Delta Q_2\rangle\left[Q_1\langle\Delta^2\mathcal{L}(t)\rangle_1 + Q_2\langle\Delta^2\mathcal{L}(t)\rangle_2\right] \\ &= -Q_1Q_2\left[Q_1V\Delta t - Q_2V\Delta t\right] + \frac{1}{2}Q_1Q_2(Q_1 - Q_2)\left[2Q_1D\Delta t + 2Q_2D\Delta t\right] \\ &= \Delta t V Q_1Q_2(Q_2 - Q_1) + \Delta t D Q_1Q_2(Q_1 - Q_2)(Q_1 + Q_2) \\ &= \Delta t Q_1Q_2(Q_1 - Q_2)(V - D), \end{aligned} \tag{31}$$

from which we derive that $V = D$.

C.6 The first passage time to decision

The first exit time of a drift-diffusion process starting from 0 with two symmetric boundaries at $+K$ and $-K$ is given by $\langle T\rangle = K\tanh(VK/2D)/V$ (see for instance [46]). Plugging in $V = D$, we recover Eq. 4 of the main text:

$$\langle T\rangle = \frac{K\tanh(K/2)}{V}. \tag{32}$$

We check that this approximation is correct for small concentration differences in Fig. 9 a, b and c. As mentioned in the main text, because the hyperbolic tangent is very flat for high values of its argument, we find that the mean decision time depends weakly on corrections to $V = D$ when the error rate e is small (which is equivalent to K large). We check that this result in true in Fig. 9 d. We note that from $K = \log(1-e)/e$ we have $\tanh(K/2) = 1 - 2e$. And so we recover the second part of Eq. 4 from the main text

$$\langle T\rangle = \frac{K}{V}(1 - 2e). \tag{33}$$

In one of the original papers about SPRT [26], Wald derives a similar formula for the total number of events before the decision:

$$\langle J_{\text{exit}}\rangle = \frac{K}{V(\tau_{\text{ON}} + \tau_{\text{OFF}})}(1 - 2e), \tag{34}$$

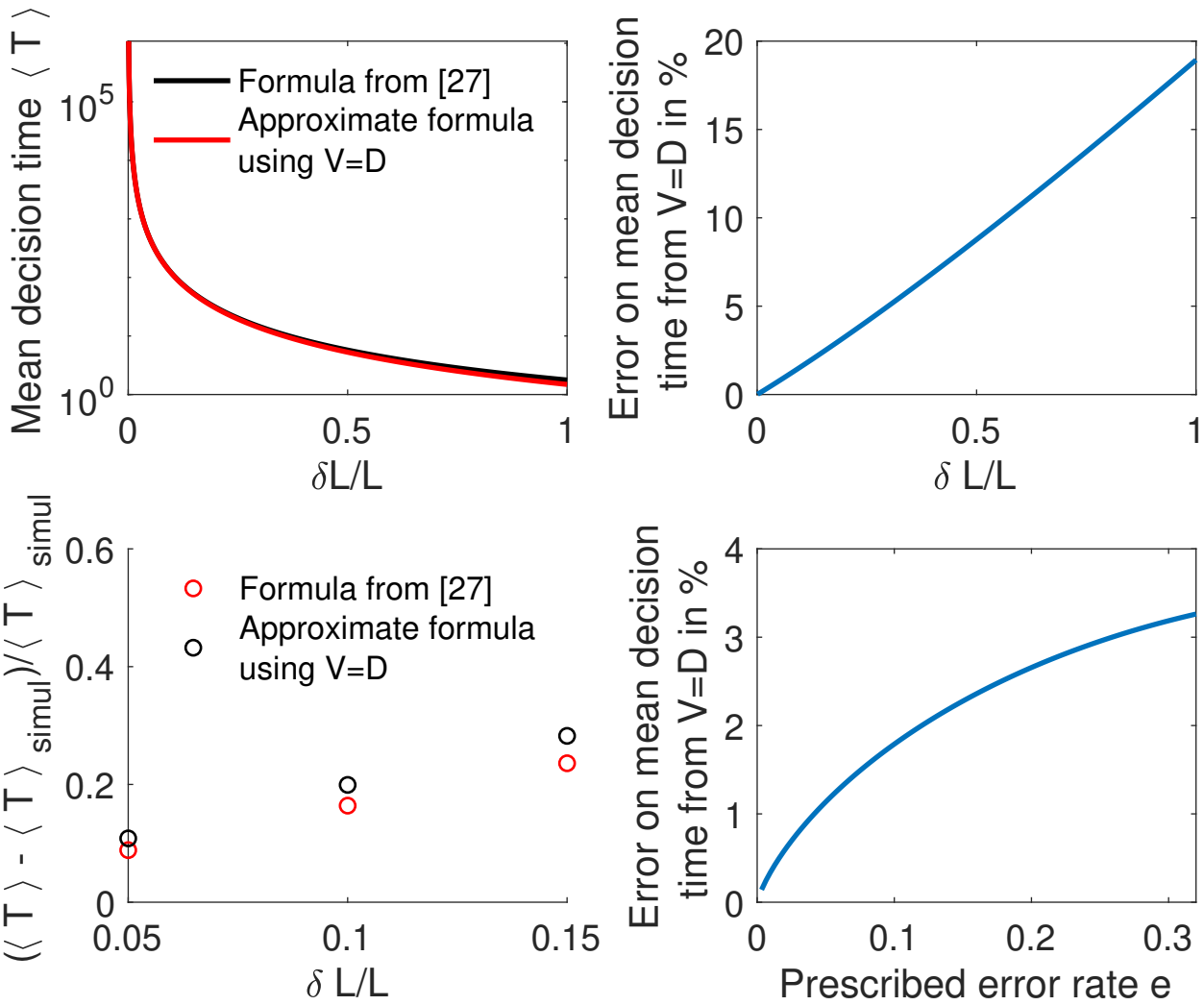

Figure 9: **Comparing methods to compute the mean decision time for the one binding site case. a.** We compute the mean decision time for one binding site using the method from [27] $\langle T\rangle_{\rm SV}$ (i.e $\langle T\rangle_{\rm SV} = K\tanh(VK/2D)/V$ and Eq. 2 and 26) in black and mean decision time $\langle T\rangle$ from the approximate method using $V = D$, Eq. 2 and Eq. 4 in red. In panel **b** we show for the same results the error made from using $V = D$: $100 * |\langle T\rangle_{\rm SV} - \langle T\rangle|/\langle T\rangle_{\rm SV}$. We find that the difference is small for small concentration differences $\delta L/L$. **c.** We show the relative error for the methods to compute the mean decision time compared to the mean time to decision $\langle T\rangle_{\rm simul}$ in a Monte-Carlo simulation. We find again that the error is small for small concentration differences. Parameters are $e = 0.32$, $L = L_2 = 1\ \mu m^{-3}$, $L_1 = L + \delta L$, $\mu = 1\ \mu m^3 s^{-1}$, $\nu = 1\ s^{-1}$. **d** We show the relative error from $V = D$ (i.e $100 * |\langle T\rangle_{\rm SV} - \langle T\rangle|/\langle T\rangle_{\rm SV}$) for fixed $\delta L/L = 0.2$ as a function of the error rate. We find that the correction to $V = D$ is weak for small errors. Other parameters are the same as **a,b,c**.

where $J_{\rm exit}$ is the number of ON-OFF events when decision happens. Combining Eq. 34 with Wald's equality [47, 48] that states that $\langle T\rangle = \langle J_{\rm exit}\rangle(\tau_{\rm ON} + \tau_{\rm OFF})$ we recover Eq. 33.

C.7 When are correlations between the times of events leading to decision important?

To compute the drift or diffusivity, one must compute the variation of the log-likelihood up to a given time T. The fact that the total time T is fixed introduces correlation between the duration of the different ON-OFF events. Can these correlations be ignored, leading to an effective drift or diffusion per cycle? They can only when the two concentrations are close, as we check in Fig. 10.

Following the arguments in [49], let us consider the following generating function for the cumulants of the log-likelihood difference $e^{\lambda(\mathcal{L}_2-\mathcal{L}_1)}$ at a given time T assuming hypothesis i is true ($i = 1$ or 2) :

$$M(\lambda) = \sum_{n=1}^{\infty} \int \left[e^{\lambda(\mathcal{L}_2-\mathcal{L}_1)} \left(\prod_{j=1}^{n} P_{\rm ON}(s_j, L_i) P_{\rm OFF}(t_j, L_i)\, dt_j\, ds_j \right) \Theta \left(T - \sum_{j=1}^{n} (t_j + s_j) \right) \right] , \tag{35}$$

where $\mathcal{L}_\alpha$ is the log-likelihood of hypothesis α, n is the number of ON-OFF cycles and s_j and t_j are respectively the ON and OFF waiting times. This is not exactly what appears in [49] but it is sufficient to grasp the consequences of the correlations introduced by a global constraint on the duration of the process, i.e. the Θ function. Note that such constraint breaks the statistical independence of the various cycles, and introduces dependencies even though the $P_{\rm ON}$ and $P_{\rm OFF}$ factorize. We rewrite the Heaviside function using the Laplace transform form $\Theta(x) = \int_{\gamma-i\infty}^{\gamma+i\infty} \frac{d\sigma}{2i\pi\sigma} e^{\sigma x}$ and the product of the probabilities as $e^{\sum p_{\rm ON}(s_j,L_\alpha)+p_{\rm OFF}(t_j,L_\alpha)}$, where $p_{\rm ON}(., L_\alpha)$ and $p_{\rm OFF}(., L_\alpha)$ are the log-likelihoods for hypothesis α. Putting the pieces together we obtain

$$M(\lambda) = \sum_{n=1}^{\infty} \int_{\gamma-i\infty}^{\gamma+i\infty} \frac{d\sigma}{2i\pi\sigma} e^{\sigma T} f^n(\sigma, \lambda) , \tag{36}$$

where

$$f(\sigma, \lambda) \equiv \int \int e^{\lambda[(p_{\rm ON}(s,L_2)-p_{\rm ON}(s,L_1))+(p_{\rm OFF}(t,L_2)-q_{\rm OFF}(t,L_2))]} \times e^{p_{\rm ON}(s,L_i)+q_{\rm OFF}(t,L_i)-\sigma(t+s)}\, dt\, ds . \tag{37}$$

One can remark that the expression is factorized, i.e. f is raised to the power n, and even f itself can be interpreted as "expectation value" of $e^{\lambda[p_{\rm ON}(s,L_2)-p_{\rm ON}(s,L_1)]}$ (and same with $p_{\rm OFF}(t, L_\alpha)$) over the "distribution" $e^{p_{\rm ON}(s,L_i)+q_{\rm OFF}(t,L_i)-\sigma(t+s)}$, i.e. the constraint introduces an exponential factor that distorts the weight of the various durations. These elements are consistent with the idea of a random variable per cycle that can be averaged to compute the drift and diffusivity. However, the idea of ignoring correlations between duration of events is not valid because σ is a function of λ. Indeed, summing the series over n gives $f(\sigma, \lambda)/(1 - f(\sigma, \lambda))$ and the asymptotic behavior is then determined by the first singularity encountered as γ is moved to the left for the inverse Laplace transform. For each value of λ, this determines a value of σ, that is $\sigma_s(\lambda)$ (see [49] for the complete calculation).

What the above says more qualitatively is that the variables per cycle are correlated because of the global constraint and there is not a single-cycle effective probability distribution that can account for that because of the dependence of σ on λ. In other words, different moments involve different configurations and distortions of the weights for the durations of the cycles. The only exception is when $d\sigma_s(\lambda)/d\lambda$ vanishes, which is the case for two close hypotheses. Indeed, from $f(\sigma_s(\lambda), \lambda) = 1$, one obtains $d\sigma_s/d\lambda \propto \partial f/\partial\lambda$ and it also holds $\partial f/\partial\lambda(\lambda = 0) = \langle (p_{\rm ON}(s, L_2) - p_{\rm ON}(s, L_1)) + (p_{\rm OFF}(t, L_2) - p_{\rm ON}(t, L_1))\rangle$. We checked explicitly in subsection C.5 that in that limit in the formula from [49] the first two terms are negligible and the diffusivity reduces to the variance of the log-likelihoods only.

Indeed, when the two hypothetical concentrations are close and the correlations can be ignored, a diffusivity per cycle can be defined naturally as

$$D_{\rm pc} = D_3 - V^2, \tag{38}$$

where D_3 is the average of the squared log-likelihood variation (see Eq. 24). We check in Fig. 10 that this formula is a good approximation for small concentration differences in the context of one binding site. In that context we have

$$D_{\rm pc} = \frac{1}{2} \frac{1}{\nu^{-1} + (\mu L)^{-1}} \left(\frac{L_1 - L_2}{L} \right)^2 , \tag{39}$$

where ν is the OFF rate and μL is the ON rate. We find that this approximation is better than the $V = D$ approximation only when the cycle times depend weakly on the concentration (i.e, for one binding site, when ν is small, see Fig. 10).

D The mean first-passage time for different architectures

Activation by multiple TF - irreversible binding all-or-nothing models. We first consider the all-or-nothing $k = 2$ two binding site cycle model depicted in Fig. 5 a.

In this model, ON events end when the complex formed by two copies of the TF unbinds. It follows that ON times are exponentially distributed and independent of the concentration $P_{\rm ON}(t) = \nu e^{-\nu t}$. Because they are independent of the concentration, they will not contribute to the log ratios. The mean ON time is given by $\tau_{\rm ON} = 1/\nu$.

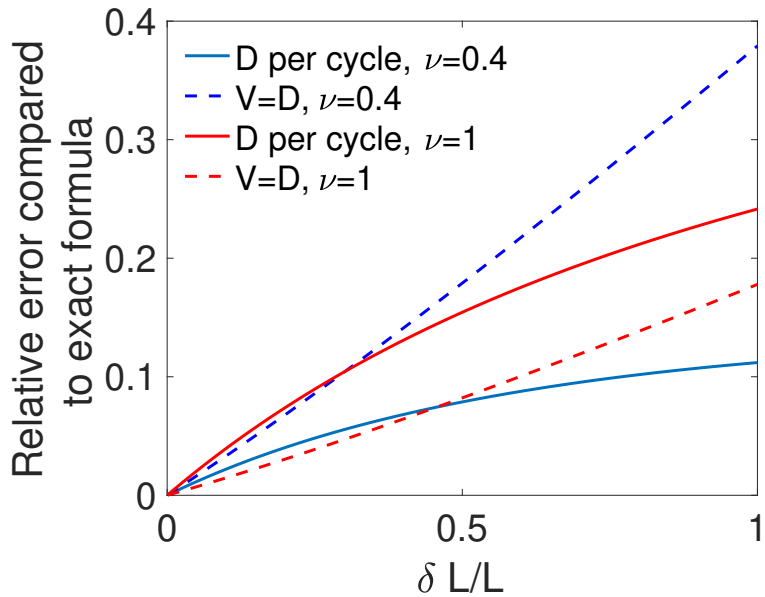

Figure 10: **Comparing two approximations for the diffusivity** For different values of the relative difference in concentrations $\delta L/L$ and for one binding site with ON rate μL and OFF rate ν, we compute the mean time to decision using the exact formula from [27] $\langle T\rangle_{\rm SV}$ (computing D according to Eq. 26), the mean time to decision computing D as a variable per cycle as in Eq. 39 $\langle T\rangle_{\rm pc}$ and the mean time per cycle using $V = D\,\langle T\rangle$. We show for both the per cycle (full lines) and the $V = D$ (dotted lines) method, the relative error made in computing the mean decision time by comparing it to the exact time $\langle T\rangle_{\rm SV}$. We find that all methods agree for small $\delta L/L$, but that the per cycle method is a better approximation only for small values of the OFF rate ν (blue curves), i.e when the times do not depend strongly on the concentration. Parameters are $e = 0.32$, $L = L_2 = 1\ \mu m^{-3}$, $L_1 = L + \delta L$, $\mu = 1\ \mu m^3 s^{-1}$.

The activation time (OFF time) requires two copies of the TF to bind and is the sum of the times it takes for each of them to bind. From a probabilistic point of view, this sum becomes a convolution and the OFF times are given by

$$\begin{aligned} P_{\rm OFF}(t,L) &= \int_0^t ds \mu_1 L e^{-\mu_1 L s} \mu_2 L e^{-\mu_2 L(t-s)} = \mu_1\mu_2 L^2 e^{-\mu_2 L t}\int_0^t ds e^{-sL(\mu_1-\mu_2)} \\ &= \mu_1\mu_2 L^2 e^{-\mu_2 L t}\frac{1}{L(\mu_2-\mu_1)}\left(e^{Lt(\mu_2-\mu_1)}-1\right) = \frac{\mu_1\mu_2 L}{\mu_2-\mu_1}\left(e^{-\mu_1 L t}-e^{-\mu_2 L t}\right). \end{aligned} \tag{40}$$

The average OFF time is $\tau_{\rm OFF} = 1/\mu_1 L + 1/\mu_2 L$.

We can now compute the drift (the ON times do not contribute to information)

$$\begin{aligned} V &= \left(\frac{1}{\mu_1 L}+\frac{1}{\mu_2 L}+\frac{1}{\nu}\right)^{-1}\int dt \frac{\mu_1\mu_2 L}{\mu_2-\mu_1}\left(e^{-\mu_1 L t}-e^{-\mu_2 L t}\right) \\ &\log\left[\frac{\mu_1\mu_2 L_1}{\mu_2-\mu_1}\left(e^{-\mu_1 L_1 t}-e^{-\mu_2 L_1 t}\right)\frac{\mu_2-\mu_1}{\mu_1\mu_2 L_2}\left(e^{-\mu_1 L_2 t}-e^{-\mu_2 L_2 t}\right)^{-1}\right] \\ &= \left(\frac{1}{\mu_1 L}+\frac{1}{\mu_2 L}+\frac{1}{\nu}\right)^{-1}\left[\log\frac{L_1}{L_2}+\int dt\frac{\mu_1\mu_2 L}{\mu_2-\mu_1}\left(e^{-\mu_1 L t}-e^{-\mu_2 L t}\right)\log\frac{e^{-\mu_1 L_1 t}-e^{-\mu_2 L_1 t}}{e^{-\mu_1 L_2 t}-e^{-\mu_2 L_2 t}}\right]. \end{aligned} \tag{41}$$

The calculations above are only valid when the two binding rates are different $\mu_1 \neq \mu_2$. Let us now assume that $\mu_1 = \mu_2$. The ON time distribution is unchanged but the OFF time distribution is now

$$P_{\rm OFF}(t,L) = \int_0^t ds \mu_1 L e^{-\mu_1 L s}\mu_2 L e^{-\mu_1 L(t-s)} = \mu_1^2 L^2 t e^{-\mu_1 L t} = \gamma(2, 1/\mu_1 L), \tag{42}$$

where we have identified $\gamma(2, 1/\mu_1 L)$, the standard Gamma distribution with exponent 2 and parameter $1/\mu_1 L$. The expression of the drift simplifies as :

$$\begin{aligned} V &= \left(\frac{1}{\mu_1 L} + \frac{1}{\mu_2 L} + \frac{1}{\nu}\right)^{-1} \int_0^{+\infty} dt \mu_1^2 L^2 t e^{-\mu_1 L t} \log \frac{\mu_1^2 L_1^2 t e^{-\mu_1 L_1 t}}{\mu_1^2 L_2^2 t e^{-\mu_1 L_2 t}} \\ &= \left(\frac{1}{\mu_1 L} + \frac{1}{\mu_2 L} + \frac{1}{\nu}\right)^{-1} \left[2 \log \frac{L_1}{L_2} + 2 \frac{L_2 - L_1}{L}\right]. \end{aligned} \tag{43}$$

When the two binding rates μ_1 and μ_2 are similar but not exactly equal the activation time distribution can be approximated by the Gamma distribution $P_{\mathrm{OFF}}(t, L) \approx \gamma\left(2, \frac{\mu_1 \mu_2 L}{\mu_2 + \mu_1}\right)$. It is then convenient to use Eq. 43 with $\frac{\mu_1 \mu_2 L}{\mu_2 + \mu_1}$ as a parameter.

Activation by multiple TF – irreversible binding with 1-or-more $k = 1$ activation. We now consider the non-equilibrium two binding site 1-or-more $k = 1$ activation model depicted in Fig. 5 b. The OFF times are exponentially distributed $P_{\mathrm{OFF}}(t, L) = \mu_1 L e^{-\mu_1 L t}$. They will contribute as in the one binding-site exponential model.

The ON times are now a convolution of a concentration-dependent exponential step with rate $\mu_2 L$ and a concentration-independent unbinding with rate ν. Their distribution is

$$P_{\mathrm{ON}}(t, L) = \int_0^t ds \mu_2 L e^{-\mu_2 L s} \nu e^{-\nu(t-s)} = \frac{\mu_2 L \nu}{\nu - \mu_2 L} \left(e^{-\mu_2 L t} - e^{-\nu t}\right). \tag{44}$$

The expression is valid for $\mu_2 L \neq \nu$ and, as previously, reduces to a γ distribution with exponent 2 in case of equality.

The corresponding drift is

$$\begin{aligned} V &= \left(\frac{1}{\mu_1 L} + \frac{1}{\mu_2 L} + \frac{1}{\nu}\right)^{-1} \left[\int_0^{\infty} dt \mu_1 L e^{-\mu_1 L t} \log \frac{\mu_1 L_1 e^{-\mu_1 L_1 t}}{\mu_1 L_2 e^{-\mu_1 L_2 t}}\right. \\ &\left. + \int_0^{\infty} dt \frac{\mu_2 L \nu}{\nu - \mu_2 L} \left(e^{-\mu_2 L t} - e^{-\nu t}\right) \log \left[\frac{\mu_2 L_1 \nu}{\nu - \mu_2 L_1} \frac{\nu - \mu_2 L_2}{\mu_2 L_2 \nu} \frac{\left(e^{-\mu_2 L_1 t} - e^{-\nu t}\right)}{\left(e^{-\mu_2 L_2 t} - e^{-\nu t}\right)}\right]\right] \\ &= \left(\frac{1}{\mu_1 L} + \frac{1}{\mu_2 L} + \frac{1}{\nu}\right)^{-1} \left[2 \log \frac{L_1}{L_2} + \frac{L_2 - L_1}{L} + \log \frac{\nu - \mu_2 L_2}{\nu - \mu_2 L_1}\right. \\ &\left. + \int_0^{\infty} dt \frac{\mu_2 L \nu}{\nu - \mu_2 L} \left(e^{-\mu_2 L t} - e^{-\nu t}\right) \log \left(\frac{e^{-\mu_2 L_1 t} - e^{-\nu t}}{e^{-\mu_2 L_2 t} - e^{-\nu t}}\right)\right]. \end{aligned} \tag{45}$$

E All-or-nothing vs 1-or-more activation

In this section we give a more detailed derivation of the result given in section 2.1.4 of the main text. Specifically, we compare two activation rules for the same promoter architecture: two binding sites with binding rates μ_1 and μ_2. We consider that the two binding sites bind TF independently so that $\mu_1 = 2\mu_2$ (there are two free targets for the first binding). The two copies of the TF unbind together with unbinding rate ν. It is a cycle model. We consider the 1-or-more $k = 1$ activation rule (Fig. 5b) and the all-or-nothing activation rule (Fig. 5 a). We will prove that the fastest activation scheme is the all-or-nothing scheme when $\mu_1 L > \nu$ and 1-or-more when $\mu_1 L < \nu$. This result corresponds to the following intuitive idea : given a choice to associate the second binding with either the first binding or the unbinding for the readout by the cell, it is more informative to convolve it with the fastest of the rates to maximize the information extracted from it. This is in general true if the time per cycle is the same for the different architectures considered.

The total time it takes to go through a cycle is the same for the two architectures: $\tau_{\mathrm{ON}} + \tau_{\mathrm{OFF}} = 1\mu_1 + 1/\mu_2 + 1/\nu$, so the difference in performance will come from the amount of information extracted per cycle. We are interested in the limit of similar concentrations, i.e. $L = L_2$ and $L_1 = L + \delta L$, $\delta L << L$. Since $D = V$ and the decision time is inversely proportional to V, it is enough to compare $V^{(\mathrm{all})}$ (the drift in the all-or-nothing scheme) with $V^{(\mathrm{one})}$ (the drift in the 1-or-more scheme) to determine the fastest architecture.

To compute $V^{(\mathrm{all})}$, we start from Eq. 41, plugging in $L_2 = L$, $L_1 = L + \delta L$ and $\mu_1 = 2\mu_2$. We expand for $\delta L/L \to 0$:

$$\begin{aligned}
V^{\mathrm{all}}\left(\tau_{\mathrm{ON}} + \tau_{\mathrm{OFF}}\right) &= \log\frac{L+\delta L}{L} + \int dt 2\mu_2 L\left(e^{-\mu_2 Lt} - e^{-2\mu_2 Lt}\right)\log\frac{e^{-2\mu_2(L+\delta L)t} - e^{-\mu_2(L+\delta L)t}}{e^{-2\mu_2 Lt} - e^{-\mu_2 Lt}} \\
&= \frac{\delta L}{L} - \frac{\delta L^2}{2L^2} + \int dt 2\mu_2 L\left(e^{-\mu_2 Lt} - e^{-2\mu_2 Lt}\right)\log\frac{e^{-\mu_2\delta Lt} - e^{-\mu_2 t(L+2\delta L)}}{1 - e^{-\mu_2 Lt}} \\
&\simeq \frac{\delta L}{L} - \frac{\delta L^2}{2L^2} + \int dt 2\mu_2 L\left(e^{-\mu_2 Lt} - e^{-2\mu_2 Lt}\right)\log\left[1 - \delta L\mu_2 t\frac{1-2e^{-\mu_2 Lt}}{1-e^{-\mu_2 Lt}} + \delta L^2\frac{\mu^2 t^2}{2}\frac{1-4e^{-\mu_2 Lt}}{1-e^{-\mu_2 Lt}}\right] \\
&\simeq \frac{\delta L}{L} - \frac{\delta L^2}{2L^2} + \int dt\mu_2 L e^{-\mu_2 Lt}\left[-2\delta L\mu_2 t\left(1 - 2e^{-\mu_2 Lt}\right)\right. \\
&\left. + \delta L^2\mu_2^2 t^2\left(1 - 4e^{-\mu_2 Lt}\right) - \delta L^2\mu_2^2 t^2\frac{\left(1-2e^{-\mu_2 Lt}\right)^2}{1-e^{-\mu_2 Lt}}\right] \\
&= \frac{\delta L}{L} - \frac{\delta L^2}{2L^2} - \frac{2\delta L}{L} + \frac{\delta L}{L} - \int dt\mu_2^3 t^2 L e^{-\mu_2 Lt}\frac{1}{e^{L\mu_2 t} - 1} = -\frac{\delta L^2}{2L^2} - \frac{2\delta L^2}{L^2} + \frac{2\zeta(3)\delta L^2}{L^2},
\end{aligned} \tag{46}$$

where ζ is the Riemann zeta function. Eventually we have

$$V^{\mathrm{all}}\left(\tau_{\mathrm{ON}} + \tau_{\mathrm{OFF}}\right) = \frac{\delta L^2}{2L^2}\left[4\zeta(3) - 5\right]. \tag{47}$$

While the expansion of V^{one} does not take a simple form in general, it can be computed for the specific value of $\mu_1 L = \nu$. When $\nu = L\mu_1 = 2L\mu_2$, $L = L_2$ and $L_1 = L + \delta L$, expanding to second order Eq. 45 becomes

$$\begin{aligned}
V^{(\mathrm{one})}\left(\tau_{\mathrm{ON}} + \tau_{\mathrm{OFF}}\right) &= 2\log\frac{L+\delta L}{L} - \frac{\delta L}{L} + \log\frac{L}{L-\delta L} \\
&+ \int_0^{+\infty} dt 2\mu_2 L\left(e^{-\mu_2 Lt} - e^{-2L\mu_2 t}\right)\log\left[\frac{\left(e^{-\mu_2(L+\delta L)t} - e^{-2L\mu_2 t}\right)}{\left(e^{-\mu_2 Lt} - e^{-2L\mu_2 t}\right)}\right] \\
&\simeq \frac{2\delta L}{L} - \frac{\delta L^2}{2L^2} + \int_0^{+\infty} dt 2\mu_2 L\left(-\delta L\mu_2 t e^{-L\mu_2 t} - \frac{\delta L^2\mu_2^2 t^2}{2}\frac{e^{-L\mu_2 t}}{1 - e^{\mu_2 Lt}}\right) \\
&= \frac{2\delta L}{L} - \frac{\delta L^2}{2L^2} - \frac{2\delta L}{L} - 2\frac{\delta L^2}{L^2} + 2\zeta(3)\frac{\delta L^2}{L^2} = V^{(\mathrm{all})}(\tau_{\mathrm{ON}} + \tau_{\mathrm{OFF}}).
\end{aligned} \tag{48}$$

We can now use the above equality and the following arguments to reach the conclusion stated at the beginning of the section. $V^{(\mathrm{all})}$ is independent of ν because no information is gained about the concentrations from the step involving unbinding. Conversely, $V^{(\mathrm{one})}$ is an increasing function of ν: as ν decreases, the unbinding part takes over in the convolution for the ON times. Since the difference between the two convolutions can only decrease as ν decreases, it becomes harder and harder to differentiate the two ON time distributions, their Kullback-Leibler divergence becomes smaller, and the drift term $V^{(\mathrm{one})}$ is reduced.

In sum, for $\nu = \mu_1 L$, $V^{(\mathrm{all})} = V^{(\mathrm{one})}$; $V^{(\mathrm{all})}$ is independent of ν whilst $V^{(\mathrm{one})}$ increases with ν. We conclude that for $\nu > \mu_1 L$, $V^{(\mathrm{one})} > V^{(\mathrm{all})}$ and the 1-or-more scheme is preferred. Conversely, for $\nu < \mu_1 L$, $V^{(\mathrm{one})} < V^{(\mathrm{all})}$ and the all-or-nothing scheme is preferred.

F Comparing one and two binding-site architectures

In this section we compare the performance of a one binding-site architecture (Fig. 5 d) to that of an equilibrium all-or-nothing $k = 2$ two binding-site architecture (Fig. 5 c). The motivation is to provide detailed explanations for the results given in subsection 2.1.5 of the main text. To rank their performance, we compare, as in the previous appendix E, the drift for the two architectures.

To do the comparison, we optimize the two binding site architecture rates μ_1, μ_2 and ν_1 for a fixed value of the error rate e, the real concentration L, the hypothetical concentrations L_1 and L_2 and the second unbinding rate ν_2. The fixed second unbinding rate sets a time scale for the process. For concreteness, we suppose that the real concentration $L = L_2$ and decision is hard $L_1 = L + \delta L$, $\delta L/L << 1$.

Decisions can be trivially sped up by increasing indefinitely all the rates to very high values. To avoid this, in the optimization process we set an upper bound to be $5s^{-1}$. We choose this upper bound to be smaller than the largest

values of ν_2 considered ($9s^{-1}$) and larger than the smaller values of ν_2 considered ($1s^{-1}$). From a biological point of view, this upper bound for the ON rates can correspond to the diffusion limited arrival rate. For the OFF rates, it can correspond to a minimum bound time required to trigger a downstream mechanism (for instance, the activation of the gene). We check in Fig. 12 that curves and effects similar to those discussed below are obtained if the upper bounds are modified.

For all values of parameters, we find that the optimal ON rates are maximal ($\mu_1 = \mu_2 = 5s^{-1}$). We observed and discussed in subsection 2.1.5 that for certain values of the parameters (ν and L), the optimal first unbinding rate ν_1 reaches the upper bound $5s^{-1}$ while for smaller values the optimal first unbinding rate remains at 0 (Fig 5 inset). The transition between the two regions is sharp. Setting ν_1 to 0 is equivalent to having an effective one binding site model because the promoter never goes back to the 0 state. For that reason we want to compare the performance of a two binding site model with parameters μ_1, μ_2, ν_1 and ν_2 to that of a one binding site model with parameters μ_2 and ν_2.

Since we are in the limit of small concentration differences, the speed of decision is set by V and $\tau = \tau_{\mathrm{ON}} + \tau_{\mathrm{OFF}}$. We denote the mean drifts of the one and the two binding-site models as $V^{(1)}$ and $V^{(2)}$, respectively. Similarly, τ_1 and τ_2 are the mean times per cycle of the two models.

The one binding-site architecture activates with rate $\mu_2 L$ and deactivates with rate ν_2. Both waiting times for ON and OFF expression states are exponential. Following results in subsection 1.2.2 of the main text, we have $\tau_1 = 1/\nu_2 + 1/(\mu_2 L)$ and $V^{(1)} = (1/\nu_2 + 1/\mu_2 L)\left[\log(L_1/L_2) + (L_2 - L_1)/L\right]$. We conclude that :

$$V^{(1)} = \left[\frac{1}{\nu_2} + \frac{1}{\mu_2 L}\right]^{-1} \left[\log\frac{L+\delta L}{L} - \frac{\delta L}{L}\right]. \tag{49}$$

In the two binding site architecture, the ON times are exponentially distributed with rate ν_2. The OFF times are more complex as they can result from several cycles from a promoter with a binding site occupied to an empty promoter before finally switching to two full binding sites and gene activation. We compute $P_{\mathrm{OFF}}(t, L)$ using the modified transition matrix of the Markov chain with the ON states acting as sinks as described in Appendix C. The OFF time distribution is given by the derivative of Eq. 12.

In the two binding site model, the transition matrix is a 3 by 3 matrix and can be diagonalized analytically to compute explicitly the exponential in Eq. 12. We set $\mu_1 L_{\mathrm{eq}} = \mu_2 L_{\mathrm{eq}} = \nu_1$ since it is always the case in the identified optimal architectures for the two binding site model (where L_{eq} is the specific value of L for which upper bounds on ν_1 and μL are equal, $L_{\mathrm{eq}} = 1\ \mu m^3$ in Fig 5 f). We compute the distribution of the OFF times explicitly and find

$$P_{\mathrm{OFF}}(L,t) = \frac{\nu_1 r}{2+8r} e^{-\frac{1}{2}\nu_1 t(1+2r+\sqrt{1+4r})} \left[1 + 4r + \sqrt{1+4r} + (1+4r-\sqrt{1+4r})e^{\sqrt{1+4r}\nu_1 t}\right], \tag{50}$$

where $r = L/L_{\mathrm{eq}}$.

Computing the mean of the distribution in Eq. 50, we find that the average time for a cycle in the two binding site architecture is

$$\tau^{(2)} = \frac{1+r}{r}\frac{1}{\nu_1 r} + \frac{1}{\nu_2}. \tag{51}$$

We can now numerically integrate $V^{(2)} = \tau^{(2)} \int P_{\mathrm{OFF}}(t,L) \log\left(P_{\mathrm{OFF}}(t,L_1)/P_{\mathrm{OFF}}(t,L)\right)$. We use this simplified formula to compare the performance of the two architectures and recover the results of Fig. 5 f. We show an example for a specific value of L, varying ν_2 in Fig 11.

G Out of equilibrium architectures and averaging over several steps

In some architectures where several copies of the TF can bind or unbind at once, there can be correlations between successive ON and OFF times. This depends on the structure of the promoter Markov chain. It is made of OFF and ON states. There can be correlations between the OFF and ON times if the chain can enter the ON state subgraph through different ON states, coming from different OFF states (or the same situation reverting ON and OFF states). In that case the time that the chain will spend in the ON state will depend on the initial entry state, and so it will depend on the OFF state from which the chain entered the ON subgraph, giving a correlation with the previous OFF time to the ON time. If the structure is particularly complex, these correlations can span over several ON-OFF cycle. We do however assume that the chain is ergodic so that they vanish at long times.

To deal with this situation, a solution is to average the contribution to the information of ON/OFF events over several ON/OFF times, until the correlation with the initial times is lost. The event in the log ratio becomes a series of ON

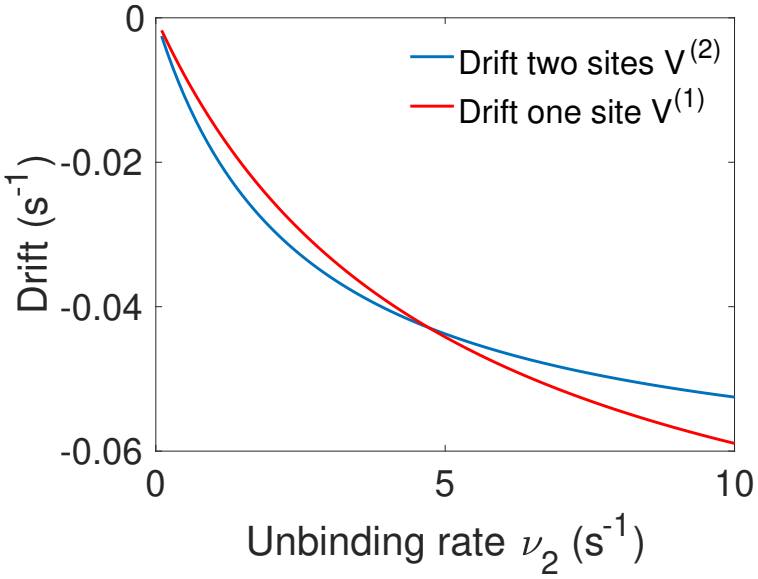

Figure 11: **Comparison of the drift for the one and two binding site equilibrium architectures** We compare the drift $V^{(1)}$ of the one binding-site architecture of Fig. 5 d and the drift $V^{(2)}$ for the two binding site equilibrium architecture of Fig 5 c. Both have the same parameters $L = L_2 = 1\mu m^{-3}$, $L_1 = 1.1\mu m^{-3}$, $\mu_1 = \mu_2 = 5\mu m^3 s^{-1}$, $\nu_1 = 5s^{-1}$ and we vary ν_2. The fastest architecture is the one with the highest absolute value of the drift (lowest on the graph). We recover the transition observed in Fig. 5 f between the optimal architectures.

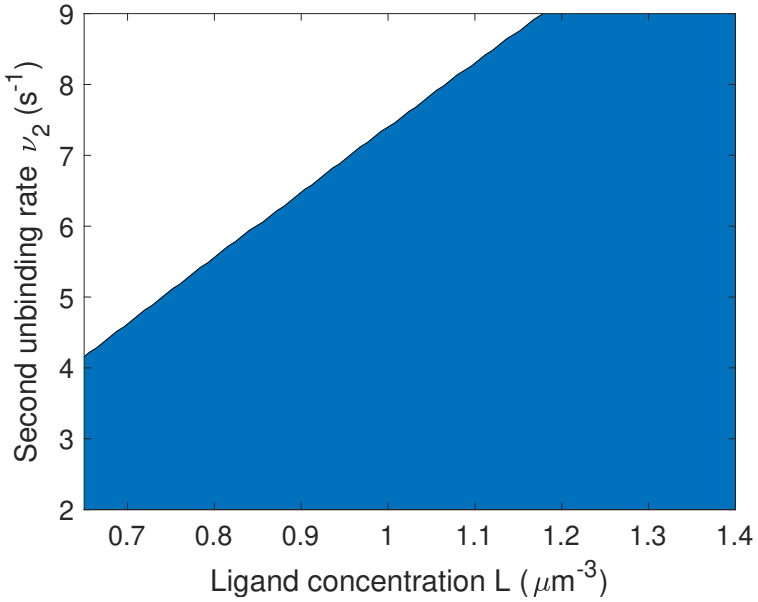

Figure 12: **Changing the bounds of the rates does not change the qualitative results on the optimal number of binding sites** We proceed as in Fig. 5 f: for a given value of L and ν we compare one- and two-binding site architectures. The blue region corresponds to two binding site promoter being optimal and the white region to one binding site promoter being optimal. Parameters are the same as in Fig. 5 f except that the upper bounds for μ_1 and μ_2 are increased to 5 $\mu m^3 s^{-1}$ and that of ν_1 is increased to $5.5s^{-1}$. We find that the results are qualitatively similar to that of Fig. 5 f. although the transition to optimal one binding site region is shifted up.

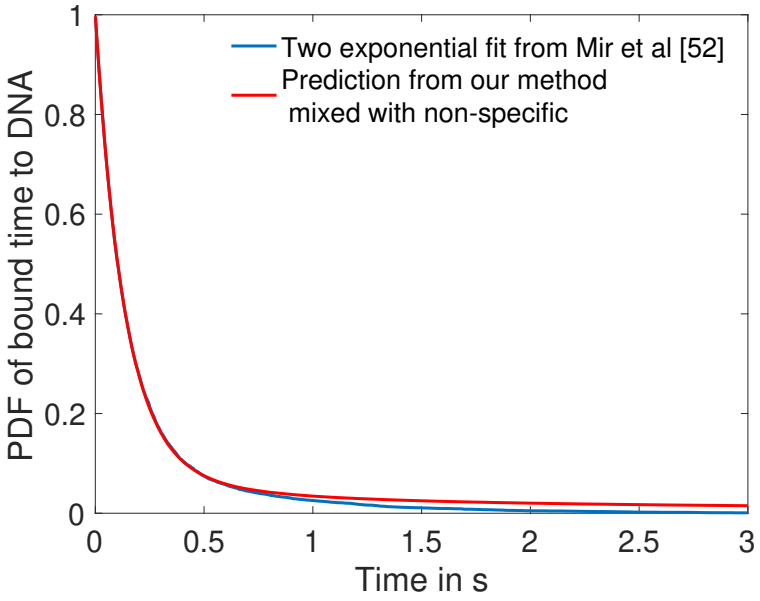

Figure 13: **Comparison of fit to data from Mir et al [52] and prediction from one of the fastest architectures for time spent bound to DNA by Bicoid molecules.** In blue we show the two exponential fit for the pdf of the time spent bound to the DNA by Bicoid molecules at the boundary for the Zelda null conditions in [52]. They fit two exponentials to the data obtaining a coefficient of determination above 0.99 for a least square fit. Their fit finds 12.9% specific traces with mean $0.629s$ and 87.1% non-specific traces with mean $0.131s$. In blue we show the PDF of time spent bound to DNA for a mix of 87.1% non-specific traces with the same mean $0.131s$ and 12.9% specific traces drawn from the distribution of time spent to DNA based on the fastest promoter architecture identified for $k = 2$, $H > 5$ (obtained from Monte Carlo simulation). Our prediction fits the blue curve from [52] with a coefficient of determination above 0.99 as well.

and OFF times and their joint probability (as they no longer factorize). The next series of events can be considered approximately (or exactly in certain cases) independent of the previous series and the rest of the theory can be applied to this sum of independent variables.

We did not explore these architectures in detail as they are extremely complex, do not seem to increase the performance of the promoter for the readout, and most likely the type of information about the concentration that is hidden in the correlation between ON and OFF would be very hard to decode for downstream mechanisms.

H Parameters for Fig. 6

Parameters for Fig.5 panel a, panel b blue full line, panel c red and panel d red are those identified as optimal for $k = 3$, $H > 4$: $\mu_1 = 0.1262\ \mu m^3 s^{-1}$, $\mu_2 = 0.1104\ \mu m^3 s^{-1}$, $\mu_3 = 0.0868\ \mu m^3 s^{-1}$, $\mu_4 = 0.0662\ \mu m^3 s^{-1}$, $\mu_5 = 0.0441\ \mu m^3 s^{-1}$, $\mu_6 = 0.0220\ \mu m^3 s^{-1}$, $\nu_1 = 1.0793 s^{-1}$, $\nu_2 = 0.5933 s^{-1}$, $\nu_3 = 0.7961 s^{-1}$, $\nu_4 = 0.5169 s^{-1}$, $\nu_5 = 0.0908 s^{-1}$, $\nu_6 = 0.1225 s^{-1}$.

Parameters for Fig.5 panel b green dashed line, panel c blue and panel d blue are those identified as optimal for $k = 2$, $H > 4$: $\mu_1 = 0.1325\ \mu m^3 s^{-1}$, $\mu_2 = 0.1088\ \mu m^3 s^{-1}$, $\mu_3 = 0.0861\ \mu m^3 s^{-1}$, $\mu_4 = 0.0662\ \mu m^3 s^{-1}$, $\mu_5 = 0.0431\ \mu m^3 s^{-1}$, $\mu_6 = 0.0215\ \mu m^3 s^{-1}$, $\nu_1 = 1.0384 s^{-1}$, $\nu_2 = 1.5926 s^{-1}$, $\nu_3 = 0.6007 s^{-1}$, $\nu_4 = 0.2966 s^{-1}$, $\nu_5 = 0.1581 s^{-1}$, $\nu_6 = 0.0947 s^{-1}$.

Other lines in panel b correspond to architectures that are close to optimality, with parameters in the same range as the ones given above.

References

[1] Bahram Houchmandzadeh, Eric Wieschaus, and Stanislas Leibler. Establishment of developmental precision and proportions in the early drosophila embryo. *Nature*, 415:798 EP –, 02 2002.

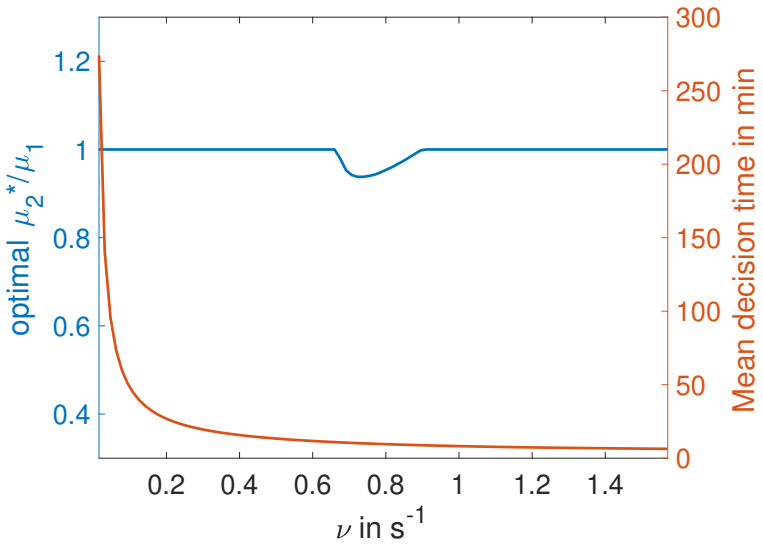

Figure 14: **Weak binding sites are optimal for a range of parameters.** In the $k = 1$, two binding site cycle architecture of Fig. 5 c, we fix ν and L and optimize for second binding rate μ_2 for a given value of μ_1, imposing $\mu_2 \leq \mu_1$. We identify the value μ_2^* for which the architecture is fastest and plot the ratio μ_2^*/μ_1. We find that for certain values of ν the second binding is not as fast as it could be, corresponding to a weaker binding site (binding probability is below 1 and the ON rate is below the diffusion limit). Parameters are $L = 0.5\ \mu m^{-3}$, $L_2 = L$, $L_1 = 0.9L$, $e = 5\%$, $\mu_1 = 1\ \mu m^3 s^{-1}$.

[2] Michael W. Perry, Jacques P. Bothma, Ryan D. Luu, and Michael Levine. Precision of hunchback expression in the Drosophila embryo. *Current Biology*, 22(23):2247–2252, 2012.

[3] Kosuke Takeda, Danying Shao, Micha Adler, Pascale G Charest, William F Loomis, Herbert Levine, Alex Groisman, Wouter-Jan Rappel, and Richard A Firtel. Incoherent feedforward control governs adaptation of activated ras in a eukaryotic chemotaxis pathway. *Science signaling*, 5(205):ra2–ra2, 01 2012.

[4] John F. Marcelletti and David H. Katz. Antigen concentration determines helper t cell subset participation in ige antibody responses. *Cellular Immunology*, 143(2):405–419, 1992.

[5] Clive G Bowsher and Peter S Swain. Environmental sensing, information transfer, and cellular decision-making. *Current Opinion in Biotechnology*, 28:149–155, 2014.

[6] Patrick H O'Farrell. Growing an Embryo from a Single Cell: A Hurdle in Animal Life. *Cold Spring Harbor Perspectives in Biology*, 7(11), nov 2015.

[7] Patrick H. O'Farrell, Jason Stumpff, and Tin Tin Su. Embryonic cleavage cycles: How is a mouse like a fly? *Current Biology*, 14(1):R35 – R45, 2004.

[8] Tanguy Lucas, Huy Tran, Carmina Angelica Perez Romero, Aurélien Guillou, Cécile Fradin, Mathieu Coppey, Aleksandra M Walczak, and Nathalie Dostatni. 3 minutes to precisely measure morphogen concentration. *PLoS Genet*, 14(10):e1007676, Oct 2018.

[9] C. Nüsslein-Volhard, E. Wieschaus, and H. Kluding. Mutations affecting the pattern of the larval cuticle indrosophila melanogaster. *Wilhelm Roux's archives of developmental biology*, 193(5):267–282, 1984.

[10] Johannes Jaeger. The gap gene network. *Cellular and Molecular Life Sciences*, 68(2):243–274, 2011.

[11] Jonathan Desponds, Huy Tran, Teresa Ferraro, Tanguy Lucas, Carmina Perez Romero, Aurelien Guillou, Cecile Fradin, Mathieu Coppey, Nathalie Dostatni, and Aleksandra M Walczak. Precision of readout at the hunchback gene: Analyzing short transcription time traces in living fly embryos. *PLoS Computational Biology*, 2016.

[12] Thomas Gregor, Eric F Wieschaus, Alistair P McGregor, William Bialek, and David W Tank. Stability and nuclear dynamics of the bicoid morphogen gradient. *Cell*, 130(1):141–52, 2007.

[13] Aude Porcher, Asmahan Abu-Arish, Sébastien Huart, Baptiste Roelens, Cecile Fradin, and Nathalie Dostatni. The time to measure positional information: maternal hunchback is required for the synchrony of the Bicoid transcriptional response at the onset of zygotic transcription. *Development*, 137(16):2795–804, 2010.

[14] Hernan G Garcia, Mikhail Tikhonov, Albert Lin, and Thomas Gregor. Quantitative imaging of transcription in living Drosophila embryos links polymerase activity to patterning. *Current Biology*, 23(21):2140–5, 2013.

[15] Mariela D. Petkova, Gašper Tkačik, William Bialek, Eric F. Wieschaus, and Thomas Gregor. Optimal decoding of cellular identities in a genetic network. *Cell*, 176(4):844–855.e15, 2019.

[16] Mikhail Tikhonov, Shawn C Little, and Thomas Gregor. Only accessible information is useful : insights from patterning Subject Category :. *Royal Society Open Science*, 2(150486), 2015.

[17] H C Berg and E M Purcell. Physics of chemoreception. *Biophysical journal*, 20(2):193–219, November 1977.

[18] William Bialek and Sima Setayeshgar. Physical limits to biochemical signaling. *Proceedings of the National Academy of Sciences*, 2005(102):10040–10045, 2005.

[19] Kazunari Kaizu, Wiet De Ronde, Joris Paijmans, Koichi Takahashi, and Filipe Tostevin. The Berg-Purcell Limit Revisited. *Biophysical journal*, 106(4):976–985, 2014.

[20] Robert G. Endres and Ned S. Wingreen. Accuracy of direct gradient sensing by single cells. *Proceedings of the National Academy of Sciences*, 105(41):15749–15754, 2008.

[21] Robert G. Endres and Ned S. Wingreen. Maximum likelihood and the single receptor. *Phys. Rev. Lett.*, 103:158101, Oct 2009.

[22] Thierry Mora and Ned S. Wingreen. Limits of sensing temporal concentration changes by single cells. *Phys. Rev. Lett.*, 104:248101, Jun 2010.

[23] Thomas Gregor, David W. Tank, Eric F. Wieschaus, and William Bialek. Probing the limits to positional information. *Cell*, 130(1):153–164, 2007.

[24] Thorsten Erdmann, Martin Howard, and Pieter Rein ten Wolde. Role of spatial averaging in the precision of gene expression patterns. *Physical Review Letters*, 103(25):258101, 2009.

[25] Gerardo Aquino, Ned S. Wingreen, and Robert G. Endres. Know the single-receptor sensing limit? think again. *Journal of Statistical Physics*, 162(5):1353–1364, 2016.

[26] A Wald. Sequential tests of statistical hypotheses. *Ann Math Stat*, 1945.

[27] Eric D Siggia and Massimo Vergassola. Decisions on the fly in cellular sensory systems. *Proceedings of the National Academy of Sciences*, 2013.

[28] Joshua I. Gold and Michael N. Shadlen. The neural basis of decision making. *Annual Review of Neuroscience*, 30(1):535–574, 2019/01/23 2007.

[29] James A. R. Marshall, Rafal Bogazc, Anna Dornhaus, Robert Planque, Tim Kovacs, and Nigel R. Franks. On optimal decision-making in brains and social insect colonies. *Journals of the Royal Society Interface*, 2009.

[30] Édgar Roldán, Izaak Neri, Meik Dörpinghaus, Heinrich Meyr, and Frank Jülicher. Decision making in the arrow of time. *Physical Review Letters*, 115(25):250602–, 12 2015.

[31] Amanda Ochoa-Espinosa, Danyang Yu, Aristotelis Tsirigos, Paolo Struffi, and Stephen Small. Anterior-posterior positional information in the absence of a strong bicoid gradient. *Proceedings of the National Academy of Sciences*, 106(10):3823, 03 2009.

[32] Gerardo Jiménez, Antoine Guichet, Anne Ephrussi, and Jordi Casanova. Relief of gene repression by torso rtk signaling: role of capicua in drosophila terminal and dorsoventral patterning. *Genes & Development*, 14(2):224–231, 01 2000.

[33] Thomas R. Sokolowski, Thorsten Erdmann, and Pieter Rein ten Wolde. Mutual repression enhances the steepness and precision of gene expression boundaries. *PLOS Computational Biology*, 8(8):e1002654–, 08 2012.

[34] Huy Tran, Jonathan Desponds, Carmina Angelica Perez Romero, Mathieu Coppey, Cecile Fradin, Nathalie Dostatni, and Aleksandra M. Walczak. Precision in a rush: Trade-offs between reproducibility and steepness of the hunchback expression pattern. *PLOS Computational Biology*, 14(10):e1006513–, 10 2018.

[35] Michael W Perry, Alistair N Boettiger, and Michael Levine. Multiple enhancers ensure precision of gap gene-expression patterns in the Drosophila embryo. *Proceedings of the National Academy of Sciences*, 108(33):1–12, 2011.

[36] Cheryll Tickle Lewis Wolpert and Alfonso Martinez Arias. *Principles of development Fifth Edition*. Oxford University Press, 2015.

[37] Wolfgang Driever and Christiane Nüsslein-Volhard. The bicoid protein determines position in the drosophila embryo in a concentration-dependent manner. *Cell*, 54(1):95–104, 1988.

[38] Gary Struhl, Paul Johnston, and Peter A. Lawrence. Control of drosophila body pattern by the hunchback morphogen gradient. *Cell*, 69(2):237–249, 1992.

[39] Olivier Crauk and Nathalie Dostatni. Bicoid determines sharp and precise target gene expression in the Drosophila embryo. *Current Biology*, 15(21):1888–98, 2005.

[40] Tanguy Lucas, Teresa Ferraro, Baptiste Roelens, Jose De Las Heras Chanes, Aleksandra M Walczak, Mathieu Coppey, and Nathalie Dostatni. Live imaging of bicoid-dependent transcription in Drosophila embryos. *Current Biology*, 23(21):2135–9, 2013.

[41] C Schröder, D Tautz, E Seifert, and H Jäckle. Differential regulation of the two transcripts from the drosophila gap segmentation gene hunchback. *The EMBO journal*, 7(9):2881–2887, 09 1988.

[42] Wolfgang Driever, Gudrun Thoma, and Christiane Nüsslein-Volhard. Determination of spatial domains of zygotic gene expression in the drosophila embryo by the affinity of binding sites for the bicoid morphogen. *Nature*, 340(6232):363–367, 1989.

[43] Gary Struhl, Kevin Struhl, and Paul M. Macdonald. The gradient morphogen bicoid is a concentration-dependent transcriptional activator. *Cell*, 57(7):1259–1273, 1989.

[44] Amanda Ochoa-Espinosa, Gozde Yucel, Leah Kaplan, Adam Pare, Noel Pura, Adam Oberstein, Dmitri Papatsenko, and Stephen Small. The role of binding site cluster strength in bicoid-dependent patterning in drosophila. *Proceedings of the National Academy of Sciences of the United States of America*, 102(14):4960, 04 2005.

[45] Javier Estrada, Felix Wong, Angela DePace, and Jeremy Gunawardena. Information Integration and Energy Expenditure in Gene Regulation. *Cell*, 166(1):234–44, 2016.

[46] Sidney Redner. *A Guide to First-Passage Processes*. Cambridge University Press, Cambridge, 2001.

[47] Abraham Wald. Some generalizations of the theory of cumulative sums of random variables. 16(3):287–293, 1945.

[48] Rick Durrett. *Probability: Theory and Examples*. Cambridge University Press, Cambridge, 2010.

[49] Martín Carballo-Pacheco, Jonathan Desponds, Tatyana Gavrilchenko, Andreas Mayer, Roshan Prizak, Gautam Reddy, Ilya Nemenman, and Thierry Mora. Receptor crosstalk improves concentration sensing of multiple ligands. *Physical Review E*, 99(2):022423–, 02 2019.

[50] Gautam Reddy, Antonio Celani, and Massimo Vergassola. Infomax strategies for an optimal balance between exploration and exploitation. *Journal of Statistical Physics*, 163(6):1454–1476, 2016.

[51] V. E. Foe and B. M. Alberts. Studies of nuclear and cytoplasmic behaviour during the five mitotic cycles that precede gastrulation in drosophila embryogenesis. *Journal of Cell Science*, 61(1):31, 05 1983.

[52] Mustafa Mir, Armando Reimer, Jenna E. Haines, Xiao Yong Li, Michael Steidler, Hernan Garcia, Michael B. Eisen, and Xavier Darzacq. Dense bicoid hubs accentuate binding along the morphogen gradient. *Genes and development*, 2017.

[53] Jeehae Park, Javier Estrada, Gemma Johnson, Chiara Ricci-Tam, Meghan Bragdon, Yekaterina Shulgina, Anna Cha, Jeremy Gunawardena, and Angela H. DePace. Dissecting the sharp response of a canonical developmental enhancer reveals multiple sources of cooperativity. *bioRxiv*, page 408708, 01 2018.

[54] Jason Gertz, Eric D. Siggia, and Barak A. Cohen. Analysis of combinatorial cis-regulation in synthetic and genomic promoters. *Nature*, 457:215 EP –, 11 2008.

[55] Christiane Nüsslein-Volhard and Eric Wieschaus. Mutations affecting segment number and polarity in drosophila. *Nature*, 287(5785):795–801, 1980.

[56] Diethard Tautz. Regulation of the drosophila segmentation gene hunchback by two maternal morphogenetic centres. *Nature*, 332(6161):281–284, 1988.

[57] Shawn C Little, Mikhail Tikhonov, and Thomas Gregor. Precise developmental gene expression arises from globally stochastic transcriptional activity. *Cell*, 154(4):789–800, 2013.

[58] Asmahan Abu-Arish, Aude Porcher, Anna Czerwonka, Nathalie Dostatni, and Cécile Fradin. High mobility of bicoid captured by fluorescence correlation spectroscopy: Implication for the rapid establishment of its gradient. *Biophysical Journal*, 99(4):33–35, 2010.

[59] Abraham Wald. On cumulative sums of random variables. *Ann. Math. Statist.*, 15(3):283–296, 1944.